ELSEVIER

Contents lists available at ScienceDirect

Quaternary Science Reviews

journal homepage: www.elsevier.com/locate/quascirev





Investigating speleothem magnetism as a proxy for dust mobilization and rainfall

Kimberly Hess^{a,*}, Roger R. Fu^a, Samuel Piascik^a, Nicolas M. Stríkis^b, Ricardo I.F. Trindade^b, Tyler Kukla^c, Alec R. Brenner^a, Plinio Jaqueto^d, Michail I. Petaev^a, Francisco W. Cruz^e, Placido Fabricio Silva Melo Buarque^f, Carlos Pérez-Mejías^g, Hai Cheng^g

- ^a Department of Earth and Planetary Sciences, Harvard University, Cambridge, MA, USA
- b Department of Geophysics, University of São Paulo, Estado de São Paulo, 05508-010, Brazil
- ^c Department of Atmospheric Sciences, University of Washington, Seattle, WA, USA
- d Institute for Rock Magnetism, University of Minnesota, Twin Cities, Minneapolis, MN, USA
- ^e Instituto de Geociências, Universidade de São Paulo, São Paulo, Brazil
- f Department of Geochemistry, Federal Fluminense University, Rio de Janeiro, 24020-141, Brazil
- g Institute of Global Environmental Change, Xi'an Jiaotong University, Xi'an, 710049, China

ARTICLE INFO

Handling editor: Mira Matthews

ABSTRACT

Commonly used speleothem-based paleoclimate proxies such as δ^{18} O. δ^{13} C. and trace element ratios are capable of high temporal resolution, but their interpretations are often ambiguous due to the conflated effects of multiple forcings. This complexity motivates the development of targeted proxies that can track specific local hydrological conditions. To this end, the concentration of ferromagnetic Fe-oxide particles in speleothem laminae has been suggested as a potential tracer for local precipitation. Here we use the quantum diamond microscope (QDM) to obtain a sub-annual resolution time series of ferromagnetic content in a Brazilian speleothem from a wellventilated cave environment covering the period between 1913 and 2016 CE. This high resolution allows us to quantify the correlation between speleothem magnetic properties and an instrumental precipitation record for the first time. We find that ferromagnetic content in the central column displays a modest but significant negative correlation with rainfall ($R^2 = 0.35$; p = 0.0027), while magnetism in the speleothem flanks shows a weaker, statistically insignificant relationship. Rock magnetic analyses of the speleothem further reveal ultrafine, pedogenic grains to be the dominant ferromagnetic carriers. Combining QDM and electron microprobe data, we show that these pedogenic grains were likely developed in surface soils and delivered into the cave as part of airborne, 10-200 µm silicate-carbonate soil agglomerates. Our results show that speleothem magnetism holds strong potential as a targeted proxy for paleorainfall and demonstrate a method for identifying the mechanism of magnetic enhancement, which sets the necessary foundation for any paleoclimatic interpretations.

1. Introduction

Speleothems are rich archives of climate processes due to their relatively continuous formation, low degree of post-depositional modification, and potential for high-precision U-series dating. The stable oxygen isotope ratio in speleothem carbonates, expressed as δ^{18} O, is the most frequently used proxy for variations in temperature and in the amount and source of precipitation over time. However, a wide range of processes and conditions spanning the oxygen isotopic composition of ocean surface water to calcite precipitation in drip water conduits in the

immediate vicinity of prior to the sampled speleothem can affect the ultimate observed δ^{18} O value (Lachniet, 2009). As a result, conflicting interpretations of speleothem δ^{18} O data are common in the literature. Tropical South America, for example, hosts some of the largest speleothem δ^{18} O shifts in the tropics, but their implications remain contentious (Cruz et al., 2009; Liu and Battisti, 2015; Wang et al., 2017; Pattnayak et al., 2019; Ampuero et al., 2020; Kukla et al., 2023). Core to this contention is the question of whether speleothem δ^{18} O is responding to local or non-local change. Non-local effects, such as upstream moisture recycling, may be prevalent in tropical δ^{18} O (Vuille et al., 2005;

^{*} Corresponding author. Department of Earth and Planetary Sciences, Harvard University, 20 Oxford Street, Cambridge, MA, 02138, USA. *E-mail address:* kimberlyhess@fas.harvard.edu (K. Hess).

Ampuero et al., 2020), but identifying them at a single site is a challenge. Partially in response to the challenge of interpreting δ¹⁸O records, other speleothem proxies have been explored as alternatives to infer local precipitation. These proxies generally posit a mechanistic link between the measured value and water infiltration to the cave (Cruz et al., 2006; Fairchild et al., 2006; Johnson et al., 2006; Partin et al., 2013; Bernal et al., 2016). For example, the chemical and isotopic systematics of several trace elements have been shown to respond to cave infiltration. In particular, variations in the Sr/Ca and Mg/Ca ratios in calcite are commonly driven by prior calcite precipitation, which may in turn be controlled by the flux of pore water entering the cave (Cruz et al., 2007). Still, other factors such as cave ventilation can impact the degree of prior calcite precipitation, while strong seasonal variations in this effect can lead to a biased record of cave hydrology (Wong et al., 2011; Oster et al., 2012, Stríkis et al., 2024).

A challenge with many other cave infiltration proxies is that they rely heavily on the cave environment and carbonate reaction pathways, which are complicated, change over time, and often require assumptions to interpret. As an example, recent studies have argued that phosphorus (P) enrichment, once posited as tracking rainfall at least in regions where it is rapidly transported through soil (Treble et al., 2003), can differ by location based on the extent of microbial mediation (Frisia et al., 2012). As another example, lead (Pb) isotopic variations may respond to infiltration changes, as enhanced erosion of overlying Pb-bearing minerals results in speleothem radiogenic Pb enrichment (Yang et al., 2015). Although robust for the studied cave, this inference relies on the occurrence of multiple, isotopically distinguishable sources in the cave vicinity.

The complications with existing rainfall proxies described above have motivated the exploration of speleothem magnetism as a proxy for past cave hydrological conditions. Decades of environmental magnetism investigations have shown that climatic variations can lead to measurable responses in the magnetic properties of sediments through their control on sediment source, deposition rate, and intensity of chemical alteration, (Verosub and Roberts, 1995). As a well-studied example, soil magnetism has been demonstrated as a robust proxy for precipitation amount in a wide range of settings where soil moisture cycling results in magnetite precipitation (Balsam et al., 2011; Maher and Possolo, 2013; Maher, 2016; Fu et al., 2023).

Critically, rock magnetic analysis can retrieve multiple dimensions of data, helping to mitigate ambiguities inherent to interpreting a single measurement. For example, a basic speleothem rock magnetic dataset may record magnetization intensities over time which, like $\delta^{18}{\rm O}$, can reflect multiple forcings. These forcings can potentially be disentangled using well-established rock magnetic techniques. Magnetic analyses of relevant properties such as grain composition and size distribution can help to pinpoint the source and delivery mechanism of magnetic particles, strengthening the interpretation of a magnetization intensity record.

These related analyses are becoming more applicable to speleothems with advances in magnetic field mapping technology, particularly the quantum diamond microscope (QDM), which permits spatial resolutions as fine as 1 μm (Glenn et al., 2017; Fu et al., 2020). For comparison, laser ablation inductively coupled plasma mass spectrometry (LA-ICP-MS), which is commonly used for generating high-resolution time series of trace element concentrations and isotopic ratios, are typically restricted to $\sim\!100~\mu m$ spot sizes. Although adequate for many purposes, $100~\mu m$ is often too coarse to resolve individual speleothem laminae. As another difference compared to LA-ICP-MS measurements, QDM magnetic field mapping produces a two-dimensional image. Such spatially resolved data can reveal grain-scale associations of ferromagnetic particles with other features and inclusions, providing further insight into the mechanism of particle enrichment and building confidence in how magnetic data are interpreted.

These potential advantages of applying rock magnetic methods to speleothems have accelerated interest in identifying links between

speleothem magnetism and past hydrological conditions. In their pioneering studies, Lascu and Feinberg (2011) and Strauss et al. (2013) used rock magnetic and electron microscopy techniques to illustrate that the dominant populations of ferrimagnetic minerals in their studied speleothems are detrital Fe-oxides and Fe-oxyhydroxides, which may in turn be controlled by cave infiltration.

A later study demonstrated a clear climatological control on speleothem magnetism by finding a robust positive correlation with $\delta^{18}{\rm O}$ and $\delta^{13}{\rm C}$ in a West Virginia speleothem (Bourne et al., 2015). The authors concluded that the production of pedogenic magnetite in the overlying soil increased during intervals of strong summer precipitation, which is associated with more enriched $\delta^{18}{\rm O}$ than winter precipitation. Following this work, Zhu et al. (2017) found a similar positive correlation between magnetism and inferred ancient rainfall in a speleothem from central China. In this case, the authors interpreted the enhancement of pedogenic magnetite flux as a consequence of increased paleo-floods during periods of strong El Niño—Southern Oscillation (ENSO) activity.

More recently, Feinberg et al. (2020) used the superconducting quantum interference device (SQUID) microscope to obtain $\sim 200~\mu m$ spatial resolution maps of a speleothem from Spring Valley Caverns, Minnesota. These measurements revealed highly magnetized flood-associated layers, demonstrating the potential for speleothem magnetism to serve as an extreme precipitation archive. Among speleothems without a history of flooding, a multiproxy study from the Italian Alps concluded that magnetization intensity correlated with enhanced delivery of pedogenic magnetite during wetter intervals, although this pattern was observed only during the late Holocene (Meghalayan) around $\sim \! 1000$ BCE (Regattieri et al., 2019). Other analyses of speleothem magnetism have cited these results to justify interpretation of stronger magnetization intensity as a proxy for higher rainfall (Chen et al., 2019).

However, several studies have shown the opposite relationship between speleothem magnetism and precipitation. Jaqueto et al. (2016) used correlations between magnetization and $\delta^{18}O$ and $\delta^{13}C$ values in a Brazilian speleothem over multi-decadal to centennial timescales to argue that magnetic particles concentrations were higher during relatively dry intervals for the last 2000 years. Here the authors proposed that vegetation retreat during such intervals would result in enhanced soil mobility and erosion, leading to increased washdown into the cave. Finally, a study of the Soreq cave in Israel showed complex variations in the magnetization – rainfall relationship in a single speleothem (Burstyn et al., 2022). Low magnetic content during the early Holocene was interpreted to be the result of high rainfall and rapid erosion suppressing soil development while a time-offset, positive correlation with $\delta^{18}O$ and $\delta^{13}C$ after 7 thousand years ago (ka) may indicate enhanced pedogenesis during moderately wetter intervals.

These previous studies demonstrate that, in every studied case, speleothem ferromagnetic content responds in some form to hydrological conditions. However, the physical driver and therefore the quantitative relationship underlying the response varies among study localities. This diversity of possible magnetic enhancement mechanisms is perhaps the central challenge preventing more widespread use of speleothem magnetism as a paleoclimatic proxy. A method or methods must be found to identify the magnetic enrichment mechanism(s) for each specific speleothem sample before any paleoclimatological information can be reliably inferred.

Here we used the QDM to characterize the environmental magnetic record of a speleothem from Central-Eastern Brazil. We first compared a sub-annual resolution time series of magnetic particle concentration to nearby rain gauge measurements to directly quantify, for the first time, the magnetization – rainfall relationship over a 103 y interval up to 2016 CE. This stands in contrast to most speleothem magnetism studies that, due to resolution limits, have relied on correlations to other paleoclimate proxies over multi-decadal to millennial timescales to infer hydrological conditions during intervals of enhanced magnetization. To

further assess the reproducibility of any observed correlation, we compared the magnetization time series from both the speleothem central column and sections of the speleothem flank over the same interval.

Finally, we use QDM magnetic field and electron microprobe maps to identify distinct ferromagnetic mineral populations in the speleothem and retrieve information about their grain composition and size distribution. Accumulated data from environmental magnetism studies show that ferromagnetic grains eroded from bedrock or formed authigenically in different settings display distinct behavior during laboratory remanence acquisition and demagnetization, even when composed of the same mineral (Egli, 2004). We therefore use the lamina-scale rock

magnetic information to infer the probable mode of formation and delivery mechanism for ferromagnetic grains. When applied to speleothem samples beyond the instrumental record, such rock magnetic analyses can yield self-contained information about the magnetic particle enrichment pathway that is critical to interpretation of their paleoenvironmental record.

2. Material and methods

2.1. The Ooncença 1 stalagmite sample

The stalagmite investigated in this study, designated Onça 1, was

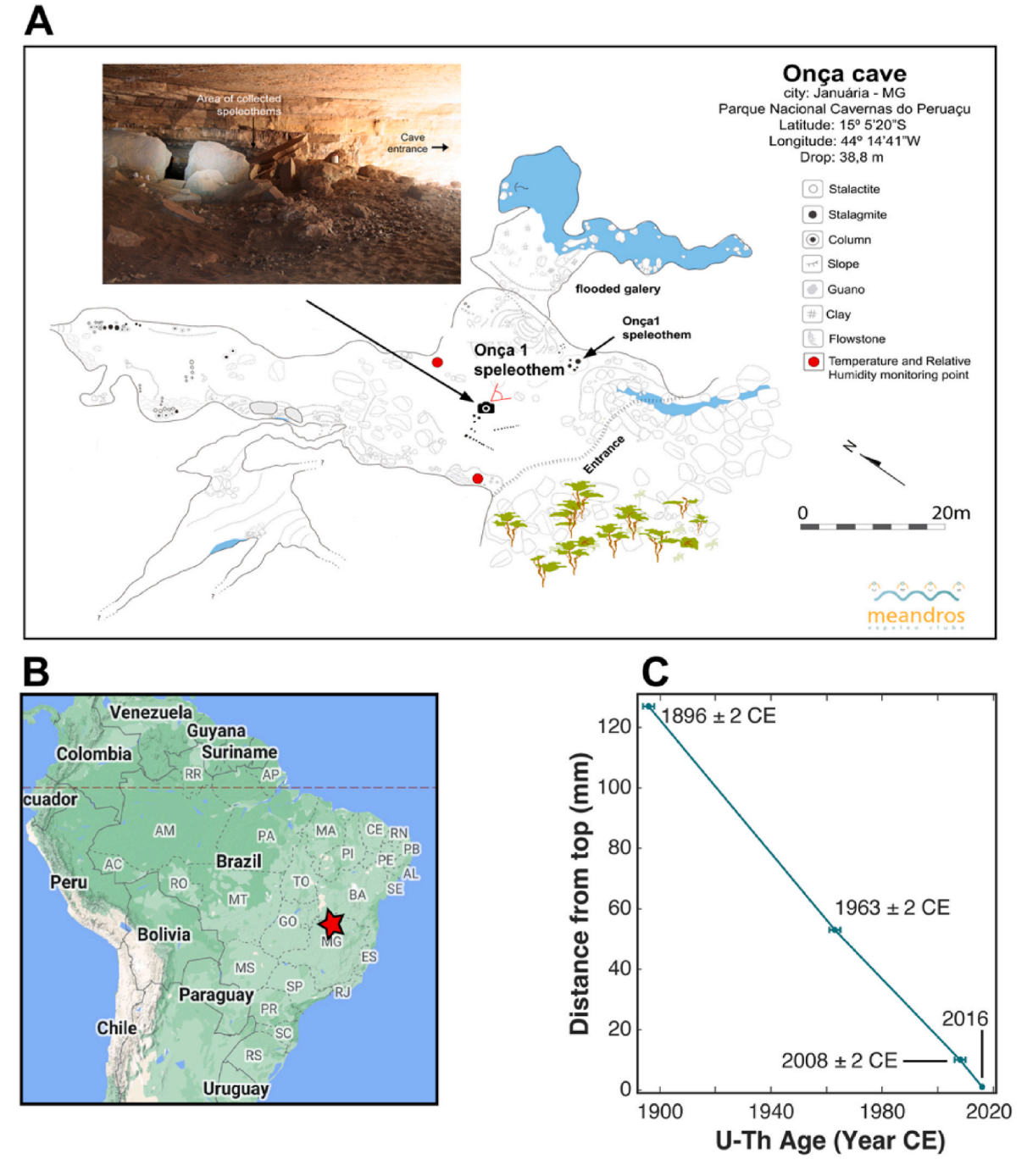


Fig. 1. Location and age model for the Onça 1 speleothem. (A) Map of the lower conduit of the Lapa da Onça cave with the Onça 1 sample site. (B) Location of Peruaçú National Park shown as star. (C) U–Th ages and uncertainties in the analyzed time interval. The final age tie point of 2016 represents the time of sampling. Lines are linear interpolation between tie points.

sampled from the Onca Cave system located in Peruacu National Park in northwestern Minas Gerais State, Brazil (15°05'19.86"S 44°14′41.39″W, Fig. 1A and B). The cave is part of the largest karstic area in Central-Eastern Brazil and formed in the Bambuí Group limestone within the Proterozoic cover sequence on the São Francisco Craton (Auler and Farrant, 1996). The cave is fed by the Peruacu River, a perennial left-bank tributary of the Rio São Francisco (IBAMA, 2003) and is situated at the base of a karst wall of approximately 100 m in height. The karst landscape of the surrounding area is characterized by valleys carved by steep slopes and towering walls of limestone. The top of limestone massif presents exposed epikarst with different karren forms. The climate in the region is tropical savanna-like with dry winters (Aw in the Köppen classification system; Peel et al., 2007). The mean annual precipitation regionally is 930 mm, with 90% falling in the spring and summer months (ONDJF) (Vera et al., 2006; Godoy-Veiga et al., 2021).

45 km southwest of the Onça Cave system is a precipitation station from *Instituto Nacional de Meteorologia* (INMET), located in the city of Januária, that began collecting data in 1913 and has maintained a reliable record since (Station OMM 83386). This record shows that, from 1913 to 2016, precipitation averaged 911 mm per calendar year with extremes of 2001 mm in 1945 and 370 mm in 1934. We selected the Onça 1 sample primarily because its age of deposition overlaps with this nearby instrumental precipitation record. When collected in 2016, Onça 1 was a 481 mm long, an actively depositing stalagmite located at a relatively short distance of only 10 m from the cave entrance and 1.6 m from surrounding cave walls (Fig. 1A). For comparison, the width of the Onça cave opening is approximately 30 m.

A cave monitoring program over the past five years has shown that cave temperature varies seasonally, oscillating from 23 $^{\circ}$ C during the warm season from October to March to 18 $^{\circ}$ C between June to August. Meanwhile, relative humidity ranges between 60% and 90% from the dry to the wet season (Stríkis et al., 2024). The Onça cave system does not have a recorded history of flooding during the deposition of our sample, supporting the assumption that particles accumulating on our sample likely entered the cave through drip water, as airborne particulates, or both. Additional cave and sampling site images are included in the supplement.

We dated the Onça 1 stalagmite using U-Th geochronology by micromilling powders from ten laminae with low apparent detrital content.

These powders were measured using ICP-MS at the Institute of Global Environmental Change, Xi'an Jiaotong University, China laboratory. Three of the U-Th samples yielded precise ages with uncertainties below 2 yrs with the most recently deposited surface having an uncertainty of 4 years - however the sampling date is known. Focusing on the four valid U-Th tie points and the active surface age between 1896 and 2016 CE, the implied mean depositional rates between tie points are relatively constant, varying between 0.97 and 1.25 mm y⁻¹ based on a York linear regression (Fig. 1C) (York et al., 2004). It is important to note that for the statistical analysis we only used the portion of the speleothem that covered the 1913-2016 timeframe due to the limitations of the precipitation record. We therefore adopted a simple age model where we applied linear interpolation in each of the three intervals between the four U-Th dated tie points. Attempts to apply layer counting as an additional age constraint were unsuccessful due to weakly and inconsistently defined layer boundaries within the sample.

To prepare the speleothem for magnetic imaging, we first cut six approximately $20 \times 5 \times 0.5$ mm thick sections along the vertical central column (Fig. 2, dashed CC line). To ensure there were no gaps in the time coverage of these sections due to kerf loss, we used a non-magnetic wire saw to cut obliquely to the laminae such that all depositional times are represented in at least one thick section. We also cut five thick sections from the flank of the speleothem that partially overlap each other in time and span the same period covered by the central column samples (Fig. 2, lines A-E, S1, S3). Here, precise relative age correlation between the central column and flank sections can be achieved by tracing visible laminae. Taking magnetic field data from both the central column and the flank of the speleothem allowed us to perform a magnetic version of the Hendy test (Hendy and Wilson, 1968) for internal reproducibility of the environmental magnetism record. We polished all thick sections using 1 µm alumina grit to obtain a flat surface for QDM magnetic field imaging. Fitting dipole models for observed magnetic sources reveals that even the weakest detectable sources with moments $\sim 1\times 10^{-16}~\text{A}$ m^2 are at least 2 µm away from the 1 µm-thick magnetic field sensing nitrogen vacancy layer, implying that they are buried at least 1 μm in the sample (Fig. S4). Stronger sources exhibit even deeper locations. This suggests that all but the very smallest grains with moments $<\sim 1 \times$ 10⁻¹⁶ A m² are located under the speleothem surface and are therefore not affected by the polishing procedure. Additional sample preparation images can be found in Fig. S3.

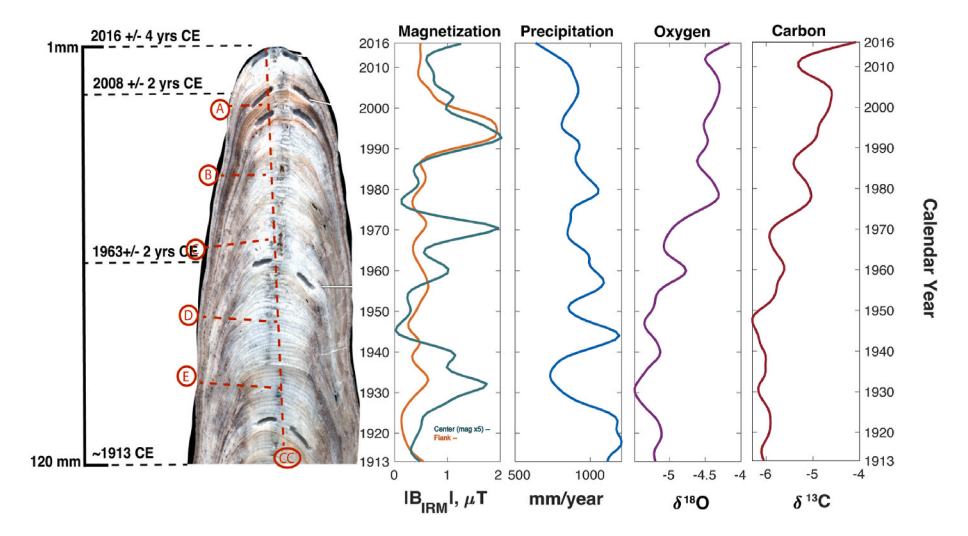


Fig. 2. Locations of magnetic profiles and time series for magnetic fields over the center column and flank of Onça1 speleothem, instrumental precipitation (INMET Strikis OMM: 83,386) and stable isotopes (raw isotope data can be found in Fig. S2) from Onça2 (Stríkis et al., 2024). Left panel shows image of the Onça 1 sample with U–Th ages 2016, 2008, 1963, 1896 (not included in this figure) referring to the visible dark segments where powder was extracted using micro milling tools. Red dashed lines represent the location of the central column ("CC") and flank sectioning ("A" through "E") measured for magnetism (see Fig. S3 for further sample preparation details). All magnetometry samples were taken from the mirror cut of the image shown and are not affected by the location of the U–Th extractions. Right panels show the indicated time series after penalized spline smoothing (see text).

2.2. Magnetic microscopy

To obtain the highest signal-to-noise ratio for the magnetic signals preserved within the speleothem, we first applied a pulsed 1 T DC magnetic field to each central column thick section pointing into the plane of section, thereby imparting a negative signed near-saturation isothermal remanent magnetization (IRM). Previous speleothem magnetism studies and our rock magnetic experiments described below show that this applied magnetic field should result in a near-saturation magnetization carried by all grains except for a small subset of goethite or fine-grained hematite (Strauss et al., 2013).

We produced the central column and flank magnetic field time series using, respectively, 65 and 42 tiled QDM fields of view, each of which had dimensions of 2.25×1.40 mm and took 35 min to acquire. All magnetic field maps were acquired under a 0.9 mT bias field that reversed twice during each imaging step, resulting in a residual effective bias field up to 400 nT. We corrected for internal reflections of global fluorescence using a factor of 0.4 appropriate for high albedo samples (Fu et al., 2020). Data was taken at 1.17 μm per pixel resolution then binned to 4.7 μm per pixel for analysis. As usual for QDM datasets, each magnetic field map was accompanied by a visible light map that is registered to the magnetic field features at pixel accuracy. This is because the same optics and camera setup is used for both magnetic field and visible light imaging while the sample remains fixed in position.

To reduce the two-dimensional QDM maps to a time series, we first manually traced visible laminae in the visible light maps using MATLAB to obtain tie points of equal age and used linear interpolation to assign a reference depth-from-top value for each pixel in the magnetic field maps. We then calculated the mean magnetic field along each group of pixels in the lamina-parallel direction to generate a single series of magnetic field values as a function of depth along the speleothem. We set all positive field values to zero to reduce the contribution from backfields produced from the strong, unidirectional IRM. To calibrate to an absolute age model, we used QDM-produced optical images registered to the magnetic field maps with pixel accuracy to wholespeleothem images that contain the radiometrically-dated tie points. This resulted in a magnetic field intensity time series containing 24,076 points, corresponding to a nominal resolution of ~1.5 days. In practice, the finite width of magnetized laminae and, more importantly, geochronological uncertainties due to uneven growth rate result in much lower effective resolution (Fig. 1C and 3, S1). We therefore performed annual binning and penalized spline smoothing of the time series prior to further data analysis, as described below in Results. We followed this procedure for both the central column and the flank sections of the speleothem. Due to the presence of traceable laminae, age calibration errors between the central column and flank time series are, for most of the time interval, limited only by the approximately annual accuracy of lamella tracing while comparisons to the instrumental rainfall time series are subject to the larger errors in radiometric ages.

As a final step in the QDM imaging process, we obtained duplicate maps of two fields of view from the speleothem central column with age $\sim\!1992\text{--}1997$ using a high-sensitivity mode on the QDM that uses microwave mixing to simultaneously resonate with the two fluorescence peaks of ^{15}N nitrogen-vacancy centers, which are split by $\sim\!3$ MHz due to hyperfine interactions (Felton et al., 2009; Levine et al., 2019). This increases the contrast of fluorescence peaks and lowers the root-mean-squared noise of the QDM maps by a factor of $\sim\!3$. These maps were able to reveal a larger proportion of dispersed magnetic sources with moments as low as 1×10^{-16} A m 2 (Fig. S4). We used these maps to assess the impact of these dispersed grains to the overall magnetic signal.

2.3. Rock magnetism and other complementary datasets

Another potential observable that may correlate with measured rainfall is the variably reddish hue of laminae, which may also track the

concentration of detrital material (Martínez-Pillado et al., 2020). To test whether red coloration could be used as an alternative proxy for precipitation, we calculated the "excess redness" in each pixel from the red and green color values (r and g, respectively) in stitched polarized optical images of the speleothem using the expression (r-g)/g. As with the magnetic timeseries, we calculated mean values of this parameter within each lamina.

To better understand how magnetic content can relate to rainfall, we sought to infer the most likely provenance of ferromagnetic phases using rock magnetic and morphological properties of Onça 1. Using both the QDM and a 2G Enterprises model 755 DC-SQuID Superconducting Rock Magnetometer (hereafter 2G SRM) at the Harvard Paleomagnetics Laboratory, we measured the anhysteretic remanent magnetization (ARM) ratio, which is defined as the saturation IRM-normalized susceptibility of ARM ($k_{\rm ARM}$ /SIRM), and the mean destructive field (MDF) of grain populations resolved in the QDM. A range of previous environmental magnetism studies have shown that these two parameters, when characterized for a single grain population, can be used to fingerprint its formation environment (Maher and Stevenson, 1988; Egli, 2004).

To retrieve the ARM ratio, we first applied an ARM with 300 mT AC and 300 µT DC fields to a speleothem flank sample and obtained a QDM magnetic field map of an area with age between 1991 and 2000 CE. We then isolated several magnetized sub-regions of this map, hereafter referred to as FLANK-FOV18, and quantified the magnetization of each sub-region using a least-squares based dipole-fitting algorithm (Fu et al., 2020). The same analysis procedure was then repeated after applying a 1 T saturation IRM to obtain the ARM ratio. To obtain the MDF of ARM, we conducted stepwise three-axis alternating field (AF) demagnetization in steps of 5-10 mT up to 80 mT after application of the same 300 mT AC field, 300 μT DC field ARM. At each AF step, we obtained a QDM magnetic field map of the same FLANK-FOV18 area and computed the magnetic moment for the same four sub-regions of interest. The MDF was then calculated by fitting a normalized AF demagnetization sequence and evaluating the AF value where the fitted magnetization falls to 0.5.

As a complementary technique to estimate grain size distributions, we used repeated ARM applications to quantify the variance in the acquired magnetization directions. For ensembles of fewer than approximately 10⁹ single domain magnetite grains, repeated applications of a thermoremanent magnetization or slowly ramped ARM should result in measurably different directions due to the finite number of recording grains (Berndt et al., 2016). A recent study of modern soils used repeated ARM directions to estimate the number of grains and, combined with the saturation IRM intensity, obtained the average size of individual grains in a several 100 µm scale regions (Fu et al., 2023). We applied a series of six ARMs with AC and DC fields of 50 and 0.3 mT, respectively, to FLANK-FOV18. This AC field level, although lower than typical for an ARM, is sufficient to saturate the fine particle population (see Results) and allowed for a slow ramp rate of 5 mT per second, which is sufficient for >80% of ≤50 nm diameter grains to experience multiple probabilistic flips and approach thermal equilibrium during ARM acquisition, see Fu et al. (2023) for derivation.

In addition to the rock magnetic experiment on FLANK-FOV18, we conducted thermal demagnetization to identify the few observed high coercivity grains. The two likely high-coercivity minerals in the cave environment are goethite and hematite, which have Néel temperatures of 120 °C and 670 °C, respectively (Dunlop and Ozdemir, 1997; Lascu and Feinberg, 2011). We therefore distinguish between them by heating the speleothem thick section up to 130 °C for 15 min in a Magnetic Measurements MMTDSC oven with <10 nT ambient field. We imaged the same field of view in the QDM after each heating to look for evidence of remagnetization. In case the high-coercivity sources were single domain or single vortex grains with a limited number of easy axes, we conducted the heating and mapping experiment three times to verify the occurrence or non-occurrence of remagnetization.

Finally, we conducted the same ARM ratio and demagnetization experiments using a 2G SRM on a $25\times5\times0.5$ mm sample from Onça 1 flank that contains FLANK-FOV18 and is designated transect "D" in Fig. 2 (Fig. S3). We obtained this bulk sample measurement to assess the contribution of any magnetic particle populations not captured in the QDM map used for rock magnetic characterization as described above. In addition to the ARM and IRM acquisition and demagnetization steps described above, we applied additional high field, three-axis AF demagnetization up to 28 mT in steps of 1–2 mT due to the presence of some higher coercivity phases in the bulk sample.

To complement our QDM-based magnetic field microscopy, we used a JEOL JXA-8230 Superprobe at the Harvard Isotope Research Geo- and Cosmochemistry Laboratory to obtain high-resolution backscatter electron maps, semi-quantitative energy dispersive spectroscopy (EDS) analyses, and wavelength dispersive spectroscopy (WDS) element maps of magnetic particle concentrations in the FLANK-FOV18 region.

2.4. Farmed calcite experiment

To monitor the calcite formation and determine the main sources of detrital particles in the surface of Onça 1 stalagmite we performed an experiment of calcite formation using concave glass surfaces (watch glasses) as an artificial substrate. To aid the nucleation of calcite crystals the concave surface of the watch glasses was pre-treated by sand-blasting. The substrates were replaced periodically every 1–2 months for 9 month June 2021–June 2023.

3. Results

3.1. An empirical magnetism-rainfall relationship

The magnetic field time series derived from both the central column and flank of Onça 1 revealed that magnetic enrichment is enhanced during years with lower measured rainfall amount (Figs. 2–4). To

quantify this relationship, we first binned the magnetic field and rainfall time series annually and smoothed using a penalized spline algorithm with spline parameter p=0.12. Penalized spline smoothing has the advantage of preserving amplitude and phase information better than a simple moving average, but the strength of smoothing can be difficult to interpret in physical time units. We therefore applied the same filter to a synthetic time series with 10, 5, and 3 y periodicities, finding that the effective smoothing window is approximately 4 or 5 y (Fig. S9). All points in the data were given equal weight in the smoothing function. We applied this level of smoothing to mitigate the effect of age model uncertainties arising from U–Th age errors and small variations in growth rate, both of which effectively limit a comparison with the instrumental record to multi-year and longer periodicities.

Correlating identically smoothed time series of measured rainfall with both central column and flank magnetic field intensity over the full 103 y overlapping interval revealed that the magnetization – rainfall relationship is stronger in the central column ($R^2=0.35$) compared to in the flank ($R^2=0.19$) (Fig. 4A and B). Autocorrelation within each time series reduces the effect number of independent observations and must be accounted for to quantify the statistical significance of each correlation. Using the implementation of the Ebisuzaki (1997) procedure of phase-randomized pseudodatasets in the *pyleoclim* software package (Khider et al., 2022), the *p*-values for the correlations are 0.0027 for the central column and 0.15 for the flank, implying that only the central column magnetization – rainfall relationship is significant. Directly comparing the magnetic field intensity of the central column and the flank showed a modest but significant correlation ($R^2=0.35$).

However, the robustness of this correlation is highly sensitive to the chosen time interval, with the large positive excursion in the 1990s detected in both time series accounting for a disproportionate part of the covariance (Fig. 4C). The larger, apparently more erratic amplitude of magnetic anomalies in the speleothem flank may be due to weaker drip water-mediated erosion, which may allow large, stochastic influxes of, for example, airborne particles to be preserved with minimal

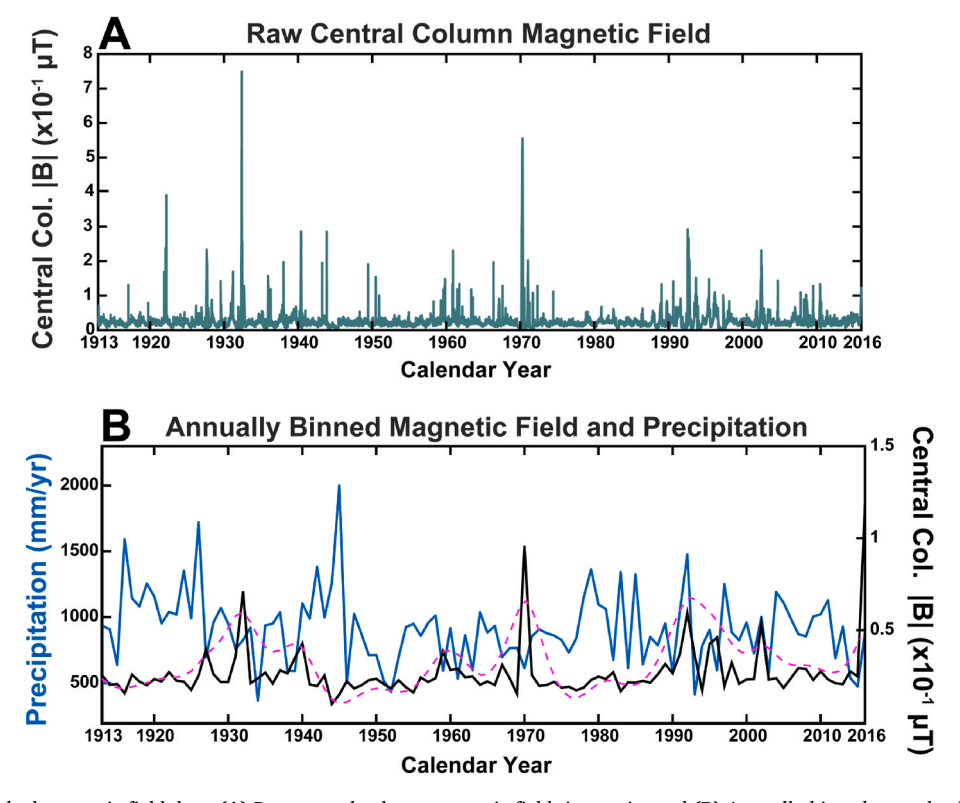


Fig. 3. Raw and unsmoothed magnetic field data. (A) Raw central column magnetic field time series and (B) Annually binned central column magnetic field time series with similarly binned precipitation records. The pink dashed line in figure B represents the smoothed magnetic data.

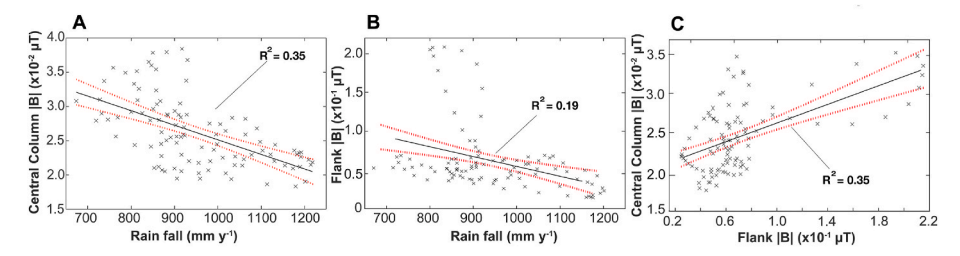


Fig. 4. Correlations between (A) central column and (B) flank magnetic fields with measured precipitation. (C) Correlation between flank and central column magnetic fields. Data points represent sampling of the penalized spline smoothed time series of both datasets at 0.5 y intervals. Black line and red curves represent the best-fit and 95% confidence interval of the ordinary least squares fit.

modification. We conclude that, although the central and flank magnetization in Onça 1 follow similar broad patterns, the signal from the central column appears to track hydrological conditions more consistently. This observed contrast between central column and flank magnetism agrees with previous studies and suggests that central column material, although typically more weakly magnetized, should be preferred for paleoclimate reconstructions (Fu et al., 2021; Shi et al., 2022).

Analyses of the high-sensitivity fields of view reveals individual ferromagnetic grains that did not appear in the standard sensitivity maps (Fig. S4). The weakest grains we identified have fitted moments between 1 and 2×10^{-16} A m² (Fu et al., 2020) which, assuming a magnetite composition, corresponds to spherical grains with diameter of ~70 nm. Therefore, even the high-sensitivity maps are likely not capturing all possible dispersed grains, some of which may be as small as ~20 nm diameter based on our analysis of magnetic carbonate-silicate agglomerates (see below for granulometry and scanning electron microscopy supporting this). Even so, at least some of the >70 nm diameter, dispersed sources in the Onça 1 sample may have a pedogenic origin given that pedogenic magnetite aggregates with sizes up to 1 μ m have been identified in other soil samples (Fu et al., 2023). At the same time, the apparently random orientations of dispersed grain magnetizations (Fig. S4C) despite the 1 T, into-the-page IRM suggests that most of these particles have high coercivities consistent with hematite or goethite and therefore most likely do not have a pedogenic origin.

In both standard- and high-sensitivity maps, the dominant magnetic signals originate from much larger, mostly laminae-bound sources, likely associated with carbonate-silicate agglomerates (Fig. S4). We therefore adopt the standard-sensitivity maps as valid approximations of the dominant magnetic signal, although variations in the concentrations of small, dispersed sources may contribute to variance and decrease the overall correlation with rainfall if they were delivered via a distinct mechanism, such as drip water, compared to the main, laminae-bound sources.

To test speleothem coloration as an alternative, more rapidly attainable proxy for detrital content, we correlated the red excess time series with rainfall, revealing no significant correlation ($R^2=0.103;p=0.234;$ Fig. 5). Interestingly, the correlation improves significantly within the 1970–2016 interval, indicating a possible shift in the mechanism controlling coloration. This finding suggests that, despite strong correlation between magnetization and coloration in other studied speleothems such as one from the Pau D'Alho Cave, Brazil (Fu et al., 2021), the latter quantity does not always track rainfall or detrital enrichment reliably and may instead be controlled by other factors such as organics and/or acid content in the drip water (Martínez-Pillado et al., 2020).

The morphologies of individual laminae are also affected by past aridity and therefore may provide independent confirmation of any magnetization – rainfall correlations. In Onça 1, we observed four layer-bounded surfaces below which laminae thin or pinch out towards the flanks over a length scale of 9–12 mm (Fig. 6). This style of lamina termination, termed Type L layer-bounded surfaces (Railsback et al., 2013), are indicative of slower growth during drier intervals. The four groups of identified Type L layer-bounded surfaces in Onça 1 correspond consistently with strongly magnetized intervals, thereby corroborating qualitatively the negative correlation between magnetization and rainfall amount. Furthermore, the L-type layer surface could create small crevasses or "traps" that are susceptible to airborne particle deposition increasing the accumulation of aeolian particles during dry periods.

3.2. Rock magnetic characterization

Having established an empirical relationship between measured magnetization and rainfall amount, we characterized the source of ferromagnetic particles in Onça 1 to aid in understanding the enrichment mechanism. We first observed the morphology of ferromagnetic mineral concentrations, focusing on FLANK-FOV18, for which other rock magnetic data are available. We found that the distribution of

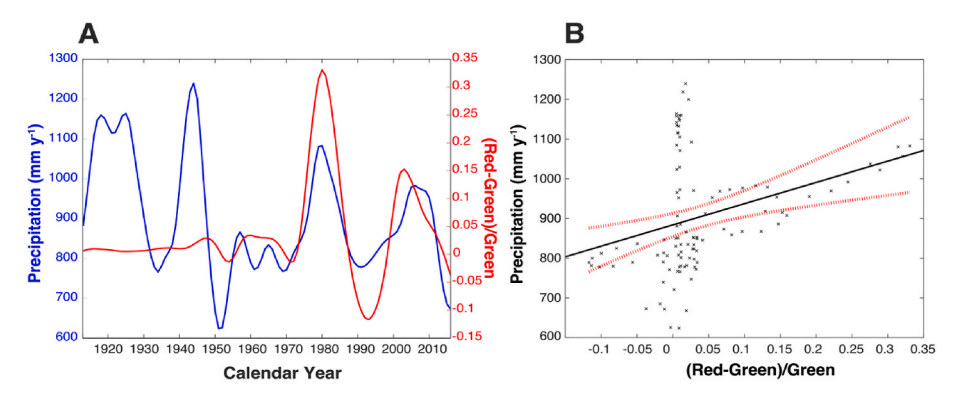


Fig. 5. Time series and correlation for speleothem color and measured precipitation. (A) Time series of the two quantities over the same time interval and after same penalized spline smoothing as the magnetic field time series in Fig. 3. (B) Correlation between speleothem color and precipitation, showing the mix of uncorrelated and well-correlated time intervals.

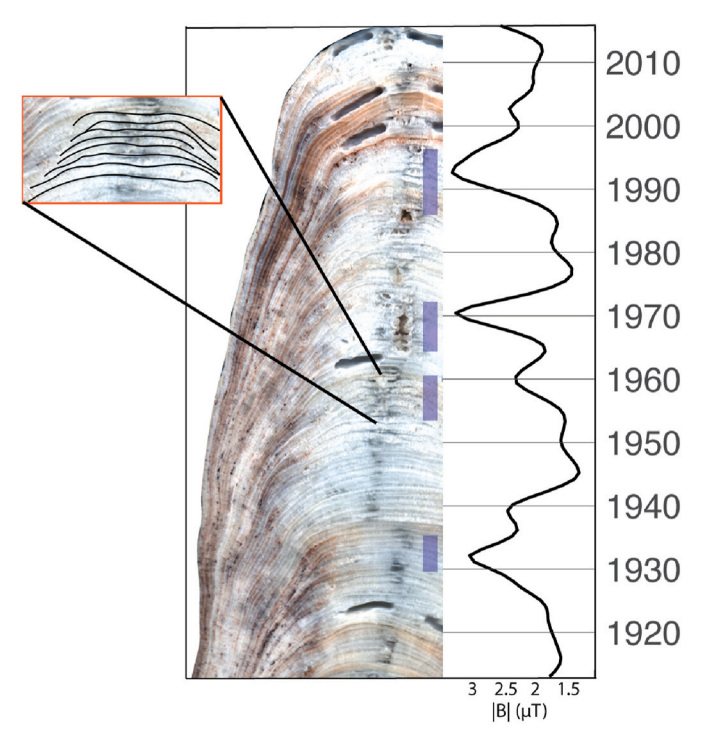


Fig. 6. Occurrences of L-type layer-bounded surfaces and relationship to central column magnetic field. Purple shading indicates intervals where laminae pinch out towards the flanks (inset), corresponding to inferred times of lower drip rate. Note qualitative correspondence with high magnetic field intervals, which also correlate with lower rainfall.

ferromagnetic material is highly heterogeneous, with strong concentrations occurring in selected laminae and no detectable signal in most time intervals (Fig. 7A). Within the highly magnetized laminae, the source distribution may be relatively uniform or highly heterogeneous, with highly localized sources separated by regions of low or null signal. Such a non-uniform distribution of ferromagnetic minerals among laminae is qualitatively similar to that observed in previously mapped speleothems from Spring Valley Caverns, Minnesota, USA and Pau d'Alho cave, Mato Grosso, Brazil (Feinberg et al., 2020; Fu et al., 2021). The presence of discrete, strongly magnetic sources indicates that a relatively small number of host particles may be responsible for the majority of magnetic enrichment and that the mechanism of their delivery is critical for understanding the overall magnetization – rainfall relationship.

Our optical and electron microscopy and EDS and WDS compositional analyses provide further details of the mineralogy of these highly magnetized host particles. Net moment inversions for the isolated ferromagnetic sources within FLANK-FOV18 can estimate the depth of the best-fit equivalent dipole source, allowing us to abrade a targeted thickness of material from the speleothem surface to reveal the source grains. Optical microscopy of the exposed ferromagnetic sources showed that the four host particles used for ARM precision-based granulometry (see below) are 40-200 µm diameter agglomerates of much smaller silicate and carbonate grains. We refer to these objects hereafter as silicate-carbonate agglomerates. Their round morphology suggests that they were transported to the speleothem as pre-formed aggregates. Backscatter electron imaging and EDS and WDS analyses reveal that the constituent particles are a heterogeneous mixture of quartz, dolomite, calcite, and clay minerals with accessory Fe-oxides (Fig. 7B). Fe element mapping reveals both strong concentrations in Fe-oxide grains and diffuse Fe that is correlated with clay minerals and anti-correlated with carbonate phases. Grain sizes range between 20 µm to the 50 nm resolution limit of the backscatter electron imaging. Small, 100 nm-scale high atomic number grains are visible but cannot be verified as

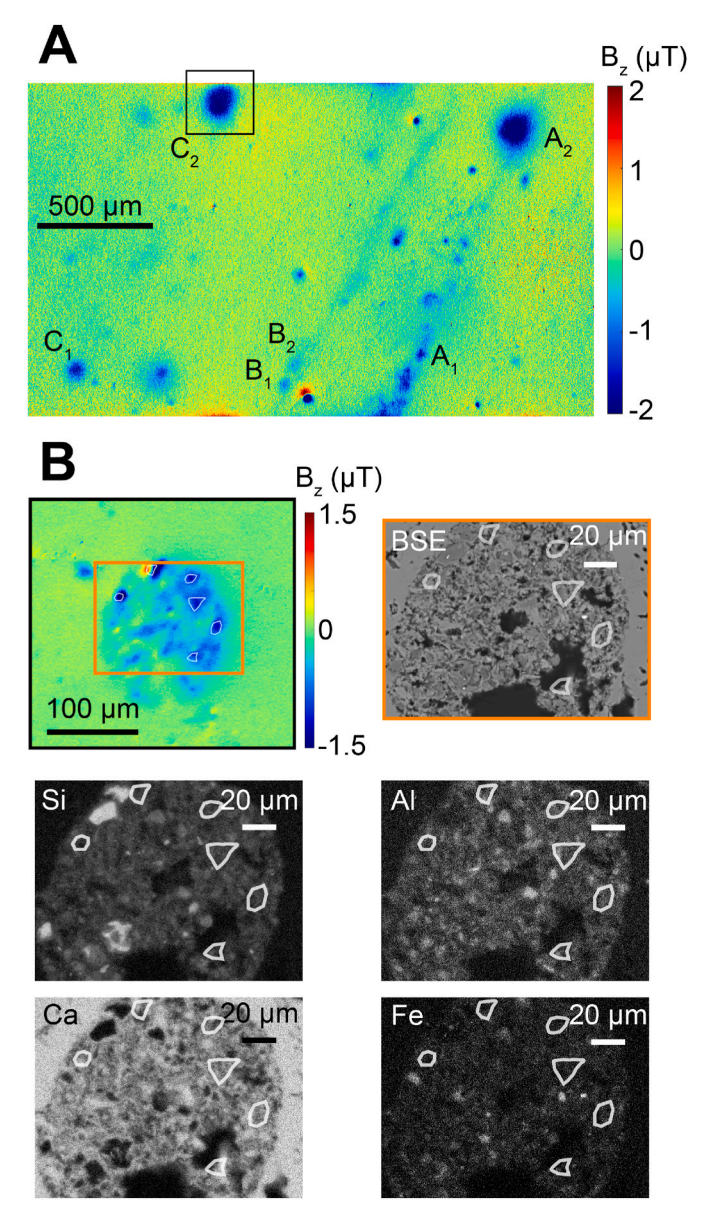


Fig. 7. QDM magnetic field and electron microprobe mapping of the FLANK-FOV18 region selected for detailed rock magnetic analysis. (A) QDM magnetic field map of a saturation IRM oriented into the page showing magnetized laminae A through C and analyzed sub-regions. Red and blue represent magnetic fields directed out of and into the page. Black box denotes the sub-region in the panel (B) QDM map. (B) QDM magnetic field and electron microprobe maps of source C_2 . Orange box in QDM map represents of the field of view of electron microscopy maps. Elemental maps are derived from WDS analysis. Small regions enclosed in light white border correspond to regions of strong magnetic fields.

ferromagnetic Fe-oxides due to their small size. Even smaller 30 nm scale ferromagnetic grains, as inferred by our granulometry experiments below, are not visible using these maps and, in any case, are unlikely to be exposed at the surface due to their very small diameters.

Although electron microprobe imaging could not directly characterize most fine Fe-oxide particles carrying the ferromagnetic signal, rock magnetic characterization could provide indirect insights into their properties. By plotting the ARM ratio against the MDF of ARM for four strongly magnetized sub-regions in FLANK-FOV18, we found that these magnetic sources show a clear affinity to previously characterized samples of pedogenic magnetite (Fig. 8A) (Egli, 2004). In contrast to the clustered, magnetostatically interacting ultrafine pedogenic magnetite

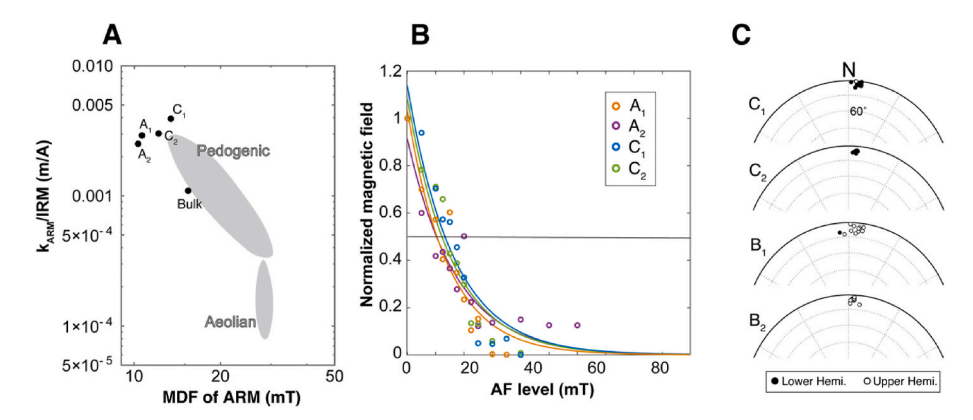


Fig. 8. Results of rock magnetic analyses. (A) MDF of ARM versus ARM ratio of magnetized sources in FLANK-FOV18 (Fig. 7). Bulk data point denotes the 62 mm^3 flank transect sample that contains FLANK-FOV18 ("D" in Fig. 2). Pedogenic and aeolian regions are based on published studies summarized in Egli (2004). (B) AF demagnetization of ARM for the four sources plotted in panel (A). Curves denote exponential fits used to determine MDF. The line at 0.5 representing when $\frac{1}{2}$ of the magnetic grains have been demagnetized. (C) Repeat ARM acquisition directions used to infer the number of nanoscale magnetic particles for the indicated sources (see Fig. 6). Sources B_1 and B_2 were used instead of A_1 and A_2 due to difficulty with dipole source fitting in the densely magnetized A lamina.

observed in QDM mapping of modern soils (Fu et al., 2023), the magnetized laminae in the Onça 1 speleothem exhibit a $\sim 6\times\,$ higher ARM ratio, which we interpret to reflect the dispersed distribution of the ultrafine magnetite grains. Similarly high ARM coercivity was also observed in a compilation of 25 other Brazilian speleothems, including five from the same Peruaçú River catchment such as Lapa da Onça (Jaqueto et al., 2021). The uniform properties of the four analyzed sub-regions, despite their occurrence in different laminae with finer, continuously distributed and coarser, discrete ferromagnetic sources strongly suggest that the fine and coarse host particles share a similar origin and emplacement mechanism, and that the magnetic enrichment pathway was stable through time.

To complement the more traditional magnetic granulometry proxies described above, we use the directional reproducibility of repeated ARM acquisitions to quantify the number of particles within each magnetized sub-region and infer the typical ferromagnetic grain size (see Section 2.3). Sets of six repeated acquisitions for each of four silicate-carbonate agglomerates with saturation IRM moment between $6\times~10^{-13}$ and $2\times$ 10^{-11} A m^2 in the FLANK-FOV18 map yielded very low angular standard deviations between 1.3° and 7.1° , which is significantly lower than those previously observed in modern, pedogenic magnetite-bearing soil samples, despite the greater overall magnetic moments of the latter (Fu et al., 2023). These high observed precisions correspond to minimum, maximum, and mean ferromagnetic grain diameters of 19, 30, and 26 nm, respectively, given a magnetite composition. These sizes are closely similar to those of transmission electron microscope-observed pedogenic magnetite nanoparticles in Chinese Loess Plateau paleosols (Ahmed and Maher, 2018). Compared to the larger, 50-140 nm inferred magnetite grain sizes in a pedogenic magnetite-bearing soil (Fu et al., 2023), these smaller sizes may result from a great degree of separation and the lack of magnetostatic interactions among them, which effectively increases the number of independent ferromagnetic domains for a given saturation magnetization. This then results in a smaller per-grain saturation magnetization and therefore smaller mean diameter. This inference is fully consistent with the result of the ARM ratio analysis described above.

The FLANK-FOV18 map also reveals several sources with coercivity between 0.3 and 1.0 T that did not remagnetize upon heating to 130 °C, suggesting a hematite composition (Fig. 7). The 3.3×10^{-13} A m^2 near-saturation IRM moment of the stronger imaged hematite-bearing particle in the lower center of the map implies a minimum grain diameter of at least 8 μm assuming a saturation magnetization of 0.25 $Am^2~kg^{-1}$ (Özdemir and Dunlop, 2014), placing these grains in a similar size range as the host agglomerates for the ultrafine pedogenic magnetite. At the same time, the high-sensitivity QDM maps obtained over the uppermost

section of the central column revealed an abundance of weak sources that were not visible in the standard-sensitivity maps (Fig. S4). The apparently randomized magnetization directions of these sources suggest that they are also composed of a high-coercivity phase.

High-resolution examination of silicate-carbonate agglomerates in the FLANK-FOV18 map after the application of a 300 mT AC field, 0.1 mT DC field ARM reveals additional coarse, high-coercivity ferromagnetic grains that did not respond to the ARM, even after multiple applications. Bulk samples that underwent the same ARM ratio and ARM demagnetization protocol revealed similar pedogenic signature combined with higher MDFs of ARM between 13 and 17.5 mT (Fig. 7A). The bulk sample rock magnetic data are therefore consistent with a combination of the two grain populations observed in QDM imaging: a dominant component consisting of pedogenic magnetite and a smaller contribution from high-coercivity hematite. The presence of two major grain populations with mean coercivities of $\sim\!15$ mT and $\sim\!100$ mT, likely representing a pedogenic magnetite and a hematite component, was further confirmed using coercivity unmixing analysis based on AF demagnetization of IRM (Fig. S5) (Maxbauer et al., 2016).

3.3. Farmed calcite experiment

Over a period of 9 months at the end of 2021, watch glasses were constantly monitored and periodically replaced on a monthly to bimonthly basis. First, the deposition of significant detrital material indicates that events of significant detrital material deposition can occur independently of flood events, which did not occur during this time. Second, we found no correlation between drip water rate and the quantity of detrital material, visible as a distinct brown coating on the watch glass surface (Fig. S8). The interval of peak particle deposition was at near the end of the dry season between early September and early November, when the drip rate was intermediate before increasing to rainy season values by February.

4. Discussion

The simultaneous availability of a well-dated speleothem with a relatively constant growth rate, a sub-annual resolution magnetization time series from QDM mapping, and a century-long instrumental rainfall record from a nearby location has permitted the first direct comparison between speleothem magnetism and recorded precipitation (Figs. 2–4). Our analysis revealed that ferromagnetic grain enrichment occurred preferentially during drier periods while rock magnetic characterization identified the ferromagnetic carrier as ultrafine pedogenic magnetite with average grain diameter of ~25 nm. These grains are hosted in

 $40\text{--}200\,\mu m$ silicate-carbonate agglomerates that are enriched in specific, highly magnetized laminae that comprise a small fraction of the total speleothem volume.

Although these results demonstrate an empirical relationship, the widespread application of the speleothem magnetism proxy would require robust identification of the mechanism of ferromagnetic grain enrichment, ideally using self-contained information that can be retrieved from each analyzed speleothem. In the case of Onça 1, the collection location in an elevated area of the conduit and the lack of adjacent sedimentary evidence for inundation can be used to rule out a flood water delivery mechanism. Furthermore, significant detrital particle deposition during the end of the dry season observed in the farmed calcite experiment further confirms the non-contribution from flooding. We now use our rock magnetic and electron microscopy data to evaluate two additional processes that may account for the episodic deposition of pedogenic magnetic horizons during drier intervals.

First, the ferromagnetic grains may have been delivered as drip water particulates and colloids, which typically refer to suspended grains smaller than 1 µm in diameter, respectively. Previous investigations have demonstrated that particles in the 10-100 nm size range characteristic of the pedogenic magnetite found in Onca 1 can be efficiently transported by pore water in karst systems (McCarthy and McKay, 2004; Hartland et al., 2012). As a potential difficulty with this model, higher rainfall and washdown may be expected to result in more intense particle deposition, contradicting the negative magnetism - rainfall relationship observed in the Onça 1 speleothem. More importantly, existing studies suggest that the dominant suspended grain population in drip water has diameter <1 µm (Hartland et al., 2011, 2012). Therefore, although drip water may transport some individual ultrafine pedogenic magnetite grains, it is not likely the source of the $40-200~\mu m$ diameter silicate-carbonate agglomerates observed to host most magnetic sources in the Onça 1 speleothem. Finally, our farmed calcite experiment observed no correlation between detrital particle deposition and drip rate (Fig. S8).

Second, we consider aeolian transport of dust particles into Onça cave. At least one previous study has documented >100 µm diameter airborne silicate particles in shallow caves (Christoforou et al., 1994). Meanwhile, >10 μm scale particles, similar to the majority of magnetic sources observed in Onça 1, have been observed in several other studied caves. Occasional measurement at the Onça 1 sampling site shows wind speed varying from 0.3 to 1 ms⁻¹ which favor the deposition of coarse aerosol particles (>100 μm) (Dredge et al., 2013). The airflow primarily moves from inside of the cave to outside but due to the proximity of the sample site external wind can occasionally be felt coming into the cave. At the same time, lower soil moisture corresponds to lower minimum wind shear stress necessary for lifting soil particles (Selah and Fryrear, 1995). This is expected to result in greater airborne dust deposition in the Onça 1 speleothem during drier intervals, which agrees with both time series analysis and layer-bounded surface observations. Combining these lines of evidence, we conclude that the silicate-carbonate agglomerates hosting ferromagnetism in the Onça 1 speleothem were delivered as airborne particulates.

Even after identifying a mechanism for silicate-carbonate agglomerate enrichment, the ferromagnetic grains themselves may have an allochthonous or autochthonous origin. In the former scenario, the pedogenic ferromagnetic grains formed in the surface soil, likely through a previous studied pathway such as redox cycling in soil pore spaces (Maher, 1998; Orgeira et al., 2011). Agglomerates of this magnetically enriched soil were then transported into the Onça cave during arid intervals. We also ruled out direct human intervention associated with land use as source of dust particles. This because the rugged topography of the surrounding areas of Onça Cave imposes major obstacles for human-settlements.

Alternatively, an autochthonous origin would imply that the soil agglomerates did not contain significant ultra-fine ferromagnetic grains upon delivery to the cave; rather, the Fe contained in non-ferromagnetic

minerals in the soil were transformed to ultrafine ferromagnets on the speleothem surface, also potentially through previously studied mechanisms. In this scenario, aridity would have modulated the total supply of mineral-bound Fe arriving in the cave through time, resulting in a more abundant Fe supply during drier intervals. Simultaneously, in situ ferromagnet growth on the speleothem, in analogy to pedogenic magnetite growth in soils, would have been accelerated during wetter intervals (Balsam et al., 2011). These two effects, one controlling Fe supply and the other controlling the rate of pedogenic reactions, would have partially offset each other. If this autochthonous origin scenario took place on the Onça 1 stalagmite, the Fe supply effect must have been dominant to result in the observed negative magnetism – rainfall relationship.

Distinguishing between the allochthonous and autochthonous origins of the ultrafine ferromagnetic grains is important for generalizing these results to other caves. The in situ formation of ultrafine ferromagnets on speleothems would introduce a novel mechanism by which hydrological conditions may influence speleothem magnetism. In this case, future speleothem environmental magnetism studies must consider potentially competing effects from in situ and delivery-mediated magnetic enhancement. Further, in situ ferromagnet growth would imply that speleothem natural remanent magnetizations are a chemical remanence while deposited, allochthonous ferromagnetic grains would carry a detrital remanent magnetization. The two magnetization mechanisms would likely result in significant differences in the ability for the speleothem to record a reliable paleomagnetic record in terms of inclination declination and absolute intensity, although relative intensities may be possible in either scenario (Ponte et al., 2017; Jaqueto et al., 2022).

Our rock magnetic analyses on FLANK-FOV18 can help distinguish allochthonous and autochthonous origins for the ultrafine, pedogenic ferromagnet population. Assuming that the rate of in situ pedogenic ferromagnet growth on a speleothem surface responds to precipitation in a similar way as in surface soils (Balsam et al., 2011), the ratio of in situ formed ultrafine ferromagnetic grains to unmodified, coarse lithogenic sources in Onça 1 laminae should also vary as a function of moisture.

In contrast, if the pedogenic magnetic grains formed allochthonously in the silicate-carbonate agglomerates prior to transport, we expect that the composition of the regional reservoir of wind-transportable dust does not vary significantly on annual timescales. In this case, the internal composition and therefore the pedogenic to lithogenic ferromagnetic content ratio, should remain constant across Onça 1 laminae.

The ARM ratio and MDF of ARM we computed for four individual silicate-carbonate agglomerates can be used to reveal any changes in the pedogenic to lithogenic grain ratio through time. The analyzed laminae A and C in FLANK-FOV18 have average magnetic field intensities that are 9.4 and 2.4 standard deviations from the mean value of the full flank time series, respectively. In fact, lamina A corresponds to the largest observed magnetic peaks, which dates to the early 1990s (Fig. S1). These laminae therefore represent a range of magnetic enrichment conditions from a typical enriched layer to one of the most intense observed enrichment events.

Among the sources in laminae A and C, we observe a uniform degree of enrichment in pedogenic magnetic particles with no sign of a spread along a mixing line towards the bulk composition and therefore no change in the ratio of pedogenic to lithogenic particles through time (Fig. 7A). Based on the reasoning above, this observation is more consistent with repeated sampling from a uniform reservoir of pedogenically enriched, wind-mobilized soil agglomerates from the outside environment and less compatible with moisture-modulated pedogenesis on the speleothem surface. We therefore conclude that the ultrafine, pedogenic grain population that dominates magnetism in Onça 1 formed external to the cave.

As stated above, this conclusion assumes that any pedogenic reactions on the speleothem surface are modulated by local moisture

availability similar to those in surface soils. This is an assumption that can be tested in future investigations of speleothem magnetism, particularly cave monitoring studies that directly compare soil particles from the speleothem, the cave interior, and exterior environment.

The analyses described here, including magnetic time series generation, lamina-scale ARM ratio and MDF of ARM quantification, ARM-based granulometry, and electron microscopy, can be repeated on any new speleothem to obtain similar insights regarding the distribution of magnetic grains and their likely origins. Full coverage of the $\sim\!98$ mm speleothem central column covering 1913–2016 CE required 65 QDM fields of view, corresponding to just under 40 h of instrument time. The 16-step demagnetization of ARM on FLANK-FOV18 required 9.3 h.

We suggest that future magnetic analyses of speleothems should conduct similar magnetic imaging to establish the sites of magnetic enrichment, which can be used, as in the case of the Onça 1 sample, to distinguish between a drip water and aeolian delivery mechanism. Further rock magnetic analyses can distinguish a pedogenic and lithogenic origin of the dominant ferromagnetic grain population, which, when tracked across laminae covering distinct environmental conditions, can distinguish between an in situ or exogenous enrichment mechanism. Combined, these insights into ferromagnetic particle origins are critical for the reliable paleoclimatic interpretation of speleothem magnetism time series for samples where, unlike Onça 1, a contemporaneous record of rainfall is not available.

Finally, we briefly analyze correlations between measured precipitation, magnetism, and δ^{18} O and δ^{13} C time series retrieved from a second speleothem (Onça 2) sampled from a well-ventilated area in the upper gallery of Onça cave. A more thorough analysis of these isotopic datasets is found in another study (Stríkis et al., 2024). We found that neither $\delta^{18}O$ or $\delta^{13}C$ records showed statistically significant correlation with either the magnetization or rain gauge measurements over the full-time studied interval. However, this lack of correlation may be attributable to competing effects caused by cave temperature and relative moisture. We observe that $\delta^{18}O$ and precipitation follow opposing trends over the 113 y interval, which is consistent with the expectation from the amount effect and has been observed in other Brazilian speleothems in regions with limited extratropical moisture sourcing (Dansgaard, 1964; Cruz et al., 2005). At the same time, we observed a positive correlation between precipitation and $\delta^{18}O$ on sub-decadal timescales. Such positive coupling may rise due kinetic isotope effects related to cave atmosphere condition, like cave relative humidity and temperature (Riechelmann et al., 2013; Stríkis et al., 2024). These observations highlight the capacity for stable isotope records to respond simultaneously to multiple forcings, which may be an advantage when these overlapping effects can be disentangled. In the absence of instrumental records, a more targeted, single pathway proxy, such as the QDM-derived magnetic field time series, can inform the interpretation of stable isotope records by quantifying, in this example, variations in local rainfall and associated dust mobilization.

5. Conclusion

The uninterrupted, rapid growth of the well-dated Onça 1 speleothem over the historical period allows QDM magnetic field imaging to construct a continuous time series of magnetic enrichment that can be directly compared to an instrumental precipitation record. This analysis reveals that magnetic enrichment in the central column exhibits a moderate negative correlation with instrumental rainfall ($R^2=0.35$), while that of flank samples are less strongly correlated ($R^2=0.19$). This result adds to the growing body of studies showing that speleothem magnetism consistently responds to local hydrological conditions, although the strength and even the sign of that relationship can vary.

To understand the physical processes underlying this correlation, we extracted lamina-scale rock magnetic properties and conducted high-resolution electron microscopy from selected regions of the Onça $\,1\,$

speleothem. Our analysis reveals that the dominant ferromagnetic particle population consists of nanoscale pedogenic grains distributed uniformly within 40–200 μm karstic soil agglomerates. The large size of the magnetic agglomerates strongly supports an aeolian delivery mechanism, which is fully compatible with the negative magnetism – rainfall relationship given higher soil mobility and erosion during dry intervals. Finally, the similar degree of pedogenic enrichments within the hosting agglomerates during wetter and drier intervals suggests that pedogenic enhancement occurred within the soil prior to deposition and not on the speleothem growth surface. The lamina-scale rock magnetic analyses described here can be applied widely to future speleothem studies to ascertain the delivery mechanism of ferromagnetic grains, thereby inferring the paleohydrological implications of any detected variations in magnetic grain concentration.

Declaration of competing interest

The authors declare that they have no known competing financial interests or personal relationships that could have appeared to influence the work reported in this paper.

Data availability

I have shared a link to the data used in this research

Acknowledgments

KH, RRF, and SP are grateful for support from the National Science Foundation (grant AGS-2202772) and the Lemann Brazil Fund. We also thank Ron Shaar and two anonymous reviewers for thoughtful comments that helped to improve the manuscript. We are grateful to the Centro Nacional de Pesquisa e Conservação de Cavernas (CECAV/ICM-Bio) for providing permission to collect stalagmite samples. This study was also financed in part by the São Paulo Research Foundation - FAPESP (grant numbers: PIRE-CREATE project 2017/50085–3) to F.W. C. and NMS; Rio de Janeiro Research Foundation – FAPERJ (grants E-26-201.421-2021 and E-26211.352-2021) to N.M.S. and Conselho Nacional de Desenvolvimento Científico e Tecnológico - CNPq (grant 312343/2022–1) to N.M.S.

Appendix A. Supplementary data

Supplementary data to this article can be found online at $\frac{\text{https:}}{\text{doi.}}$ org/10.1016/j.quascirev.2024.108598.

References

Ahmed, I.A.M., Maher, B.A., 2018. Identification and paleoclimatic significance of magnetite nanoparticles in soils. Proc. Natl. Acad. Sci. USA 115, 1736–1741. https://doi.org/10.1073/pnas.1719186115.

Ampuero, A., et al., 2020. The forest effects on the isotopic composition of rainfall in the northwestern Amazon Basin. J. Geophys. Res. Atmos. 125 (4), e2019JD031445 (2020.

Auler, A., Farrant, A.R., 1996. A brief introduction to karst and caves in Brazil. Proc. - Univ. Bristol Spelaeol. Soc. 20, 187–200.

Balsam, W.L., Ellwood, B.B., Ji, J., Williams, E.R., Long, X., El Hassani, A., 2011. Magnetic susceptibility as a proxy for rainfall: worldwide data from tropical and temperate climate. Quat. Sci. Rev. 30, 2732–2744. https://doi.org/10.1016/j.quascirev.2011.06.002.

Bernal, J.P., Cruz, F.W., Stríkis, N.M., Wang, X., Deininger, M., Catunda, M.C.A., Ortega-Obregón, C., Cheng, H., Edwards, R.L., Auler, A.S., 2016. High-resolution Holocene south American monsoon history recorded by a speleothem from botuverá cave, Brazil. Earth Planet Sci. Lett. 450, 186–196. https://doi.org/10.1016/j.epsl.2016.06.008.

Berndt, T., Muxworthy, A.R., Fabian, K., 2016. Does size matter? Statistical limits of paleomagnetic field reconstruction from small rock specimens. J. Geophys. Res. Solid Earth 121, 15–26. https://doi.org/10.1002/2015JB012441.

Bourne, M.D., Feinberg, J.M., Strauss, B.E., Hardt, B., Cheng, H., Rowe, H.D., Springer, G., Edwards, R.L., 2015. Long-term changes in precipitation recorded by magnetic minerals in speleothems. Geology 43, 595–598.

- Burstyn, Y., Shaar, R., Keinan, J., Ebert, Y., Ayalon, A., Bar-Matthews, M., Feinberg, J.M., 2022. Holocene wet episodes recorded by magnetic minerals in stalagmites from Soreq Cave. Israel: Geology 50, 284–288. https://doi.org/10.1130/G49383.1.
- Chen, Q., Zhang, T.W., Wang, Y.T., Zhao, J.X., Feng, Y.X., Liao, W., Wang, W., Yang, X. Q., 2019. Magnetism signals in a stalagmite from southern China and reconstruction of paleorainfall during the interglacial-glacial transition. Geophys. Res. Lett. 46, 6918–6925. https://doi.org/10.1029/2019GL082204.
- Christoforou, C.S., Salmon, L.G., Cass, G.R., 1994. Deposition of atmospheric particles within the Buddhist cave temples at Yungang, China. Atmos. Environ. 28, 2081–2091. https://doi.org/10.1016/1352-2310(94)90475-8.
- Cruz, F.W., Burns, S.J., Jercinovic, M., Karmann, I., Sharp, W.D., Vuille, M., 2007. Evidence of rainfall variations in Southern Brazil from trace element ratios (Mg/Ca and Sr/Ca) in a Late Pleistocene stalagmite. Geochem. Cosmochim. Acta 71, 2250–2263.
- Cruz, F.W., Burns, S.J., Karmann, I., Sharp, W.D., Vuille, M., 2006. Reconstruction of regional atmospheric circulation features during the late Pleistocene in subtropical Brazil from oxygen isotope composition of speleothems: earth Planet. Sci. Lett. 248, 405, 507
- Cruz, F.W., Karmann, I., Viana, O., Burns, S.J., Ferrari, J.A., Vuille, M., Sial, A.N., Moreira, M.Z., 2005. Stable isotope study of cave percolation waters in subtropical Brazil: implications for paleoclimate inferences from speleothems. Chem. Geol. 220, 245–262. https://doi.org/10.1016/j.chemgeo.2005.04.001.
- Cruz, F.W., Vuille, M., Burns, S.J., Wang, X., Cheng, H., Werner, M., Lawrence Edwards, R., Karmann, I., Auler, A.S., Nguyen, H., 2009. Orbitally driven east–west antiphasing of South American precipitation. Nat. Geosci. 2, 210–214. https://doi. org/10.1038/ngeo444.
- Dansgaard, W., 1964. Stable isotopes in precipitation. Tellus 16, 436-468.
- Dredge, J., Fairchild, I.J., Harrison, R.M., Fernandez-Cortes, A., Sanchez-Moral, S., Jurado, V., Gunn, J., Smith, A., Spötl, C., Mattey, D., Wynn, P.M., 2013. Cave aerosols: distribution and contribution to speleothem geochemistry. Quaternary Science Reviews 63, 23–41.
- Dunlop, D.J., Ozdemir, O., 1997. Rock Magnetism: Fundamentals and Frontiers. Cambridge University Press, Cambridge Studies in Magnetism., New York, p. 573.
- Ebisuzaki, W., 1997. A method to estimate the statistical significance of a correlation when the data are serially correlated. J. Clim. 10, 2147–2153. https://doi.org/10.1175/1520-0442(1997)010<2147:AMTETS>2.0.CO;2.
- Egli, R., 2004. Characterization of individual rock magnetic components by analysis of remanence curves: 1. Unmixing natural sediments: Studia Geophys. Geod. 48, 201 446
- Fairchild, I.J., Smith, C.L., Baker, A., Fuller, L., Spötl, C., Mattey, D., McDermott, F., M F, E.I., 2006. Modification and preservation of environmental signals in speleothems. Earth Sci. Rev. 75, 105–153. https://doi.org/10.1016/j.earscirev.2005.08.003.
- Feinberg, J.M., Lascu, I., Lima, E.A., Weiss, B.P., Dorale, J.A., Alexander, E.C., Edwards, R.L., 2020. Magnetic detection of paleoflood layers in stalagmites and implications for historical land use changes: earth Planet. Sci. Lett. 530, 115946.
- Felton, S., Edmonds, A.M., Newton, M.E., Martineau, P.M., Fisher, D., Twitchen, D.J., Baker, J.M., 2009. Hyperfine interaction in the ground state of the negatively charged nitrogen vacancy center in diamond. Phys. Rev. B 79, 075203. https://doi. org/10.1103/PhysRevB.79.075203.
- Frisia, S., Borsato, A., Drysdale, R.N., Paul, B., Greig, A., Cotte, M., 2012. A re-evaluation of the palaeoclimatic significance of phosphorus variability in speleothems revealed by high-resolution synchrotron micro XRF mapping. Clim. Past 8, 2039–2051. https://doi.org/10.5194/cp-8-2039-2012.
- Fu, R.R., Hess, K., Jaqueto, P., Novello, V.F., Kukla, T., Trindade, R.I.F., Stríkis, N.M., Cruz, F.W., Ben Dor, O., 2021. High-resolution environmental magnetism using the quantum diamond microscope (QDM): application to a tropical speleothem. Front. Earth Sci. 8, 604505, https://doi.org/10.3280/fors.2020.64505.
- Earth Sci. 8, 604505 https://doi.org/10.3389/feart.2020.604505.
 Fu, R.R., Lima, E.A., Volk, M.W.R., Trubko, R., 2020. High sensitivity moment magnetometry with the quantum diamond microscope. G-cubed 21 e2020GC009147.
- Fu, R.R., Maher, B.A., Nie, J., Gao, P., Berndt, T., Folsom, E., Cavanaugh, T., 2023. Pinpointing the mechanism of magnetic enhancement in modern soils using highresolution magnetic field imaging. G-cubed 24. https://doi.org/10.1029/ 2022GC010812
- Glenn, D.R., Fu, R.R., Kehayias, P., Sage, D.L., Lima, E.A., Weiss, B.P., Walsworth, R.L., 2017. Micrometer-scale magnetic imaging of geological samples using a quantum diamond microscope. G-cubed 18, 3254–3267. https://doi.org/10.1002/ 2017GC006946.
- Godoy-Veiga, M., Cintra, B.B.L., Stríkis, N.M., Cruz, F.W., Grohmann, C.H., Santos, M.S., Regev, L., Boaretto, E., Ceccantini, G., Locosselli, G.M., 2021. The value of climate responses of individual trees to detect areas of climate-change refugia, a tree-ring study in the Brazilian seasonally dry tropical forests. For. Ecol. Manag. 488, 118971 https://doi.org/10.1016/j.foreco.2021.118971.
- Hartland, A., Fairchild, I.J., Lead, J.R., Borsato, A., Baker, A., Frisia, S., Baalousha, M., 2012. From soil to cave: transport of trace metals by natural organic matter in karst dripwaters. Chem. Geol. 304–305, 68–82. https://doi.org/10.1016/j. chemgeo.2012.01.032.
- Hartland, A., Fairchild, I.J., Lead, J.R., Zhang, H., Baalousha, M., 2011. Size, speciation and lability of NOM-metal complexes in hyperalkaline cave dripwater. Geochem. Cosmochim. Acta 75, 7533–7551. https://doi.org/10.1016/j.gca.2011.09.030.
- Hendy, C.H., Wilson, A.T., 1968. Palaeoclimatic data from speleothems. Nature 219, 48–51. https://doi.org/10.1038/219048a0.
- IBAMA, 2003. Plano de Manejo Parque Nacional Cavernas de Peruaçú. Encarte 3 -Análise da unidade de conservação. https://www.gov.br/icmbio/pt-br/assuntos/b iodiversidade/unidade-de-conservacao/unidades-de-biomas/cerrado/lista-

- de-ucs/parna-cavernas-do-peruacu/arquivos/parna_cavernas_peruacu_pm_enc3_an exos1.pdf.
- Jaqueto, P., et al., 2022. Stalagmite paleomagnetic record of a quiet mid-to-late Holocene field activity in central South America. Nat. Commun. 13, 1349. https://doi.org/ 10.1038/s41467-022-28972-8.
- Jaqueto, P., Trindade, R.I.F., Feinberg, J.M., Carmo, J., Novello, V.F., Stríkis, N.M., Cruz, F.W., Shimizu, M.H., Karmann, I., 2021. Magnetic mineralogy of speleothems from tropical-subtropical sites of south America. Front. Earth Sci. 9, 634482 https://doi.org/10.3389/feart.2021.634482.
- Jaqueto, P., Trindade, R.I.F., Hartmann, G.A., Novello, V.F., Cruz, F.W., Karmann, I., Strauss, B.E., Feinberg, J.M., 2016. Linking speleothem and soil magnetism in the Pau d'Alho cave (central South America). J. Geophys. Res. Solid Earth 121, 7024-7039
- Johnson, K.R., Ingram, B.L., Sharp, W.D., Zhang, P., 2006. East asian summer monsoon variability during marine isotope stage 5 based on speleothem δ18O records from wanxiang cave, central China: palaeogeography, palaeoclimatology. Palaeoecology 236, 5–19. https://doi.org/10.1016/j.palaeo.2005.11.041.
- Khider, D., Emile-Geay, J., Zhu, F., James, A., Landers, J., Ratnakar, V., Gil, Y., 2022. Pyleoclim: paleoclimate timeseries analysis and visualization with Python. Paleoceanogr. Paleoclimatol. 37 https://doi.org/10.1029/2022PA004509 e2022PA004509.
- Kukla, T., Winnick, M.J., Laguë, M.M., Xia, Z., 2023. The zonal patterns in late quaternary tropical south American precipitation. Paleoceanogr. Paleoclimatol. 38 https://doi.org/10.1029/2022PA004498 e2022PA004498.
- Lachniet, M., 2009. Climatic and environmental controls on speleothem oxygen-isotope values. Quat. Sci. Rev. 28, 412–432.
- Lascu, I., Feinberg, J.M., 2011. Speleothem magnetism. Quat. Sci. Rev. 30, 3306–3320.
- Levine, E.V., Turner, M.J., Kehayias, P., Hart, C.A., Langellier, N., Trubko, R., Glenn, D. R., Fu, R.R., Walsworth, R.L., 2019. Principles and techniques of the quantum diamond microscope. Nanophotonics 8, 1945–1973. https://doi.org/10.1515/nanoph-2019-0209.
- Liu, X., Battisti, D.S., 2015. The influence of orbital forcing of tropical insolation on the climate and isotopic composition of precipitation in south America. J. Clim. 28, 4841–4862. https://doi.org/10.1175/JCLI-D-14-00639.1.
- Maher, B.A., 1998. Magnetic properties of modern soils and Quaternary loessic paleosols: paleoclimatic implications. Palaeogeogr. Palaeoclimatol. Palaeoecol. 137, 25–54. https://doi.org/10.1016/S0031-0182(97)00103-X.
- Maher, B.A., 2016. Palaeoclimatic records of the loess/palaeosol sequences of the Chinese Loess Plateau. Quat. Sci. Rev. 154, 23–84. https://doi.org/10.1016/j. quascirev.2016.08.004.
- Maher, B.A., Possolo, A., 2013. Statistical models for use of palaeosol magnetic properties as proxies of palaeorainfall. Global Planet. Change 111, 280–287.
- Maher, K.A., Stevenson, D.J., 1988. Impact frustraction of the origin of life. Nature 331, 612-614.
- Martínez-Pillado, V., Yusta, I., Iriarte, E., Álvaro, A., Ortega, N., Aranburu, A., Arsuaga, J. L., 2020. The red coloration of Goikoetxe Cave's speleothems (Busturia, Spain): an indicator of paleoclimatic changes. Quat. Int. https://doi.org/10.1016/j. quaint.2020.04.006. S1040618220301701.
- Maxbauer, D.P., Feinberg, J.M., Fox, D.L., 2016. Magnetic mineral assemblages in soils and paleosols as the basis for paleoprecipitation proxies: a review of magnetic methods and challenges. Earth Sci. Rev. 155, 28–48. https://doi.org/10.1016/j. earscirev.2016.01.014.
- McCarthy, J.F., McKay, L.D., 2004. Colloid transport in the subsurface: past, present, and future challenges. Vadose Zone J. 3, 326–337. https://doi.org/10.2136/ vzj2004.0326.
- Orgeira, M.J., Egli, R., Compagnucci, R., 2011. A quantitative model of magnetic enhancement in loessic soils. In: The Earth's Magnetic Interior. Springer, Dordrecht, pp. 361–397.
- Oster, J.L., Montañez, I.P., Kelley, N.P., 2012. Response of a modern cave system to large seasonal precipitation variability. Geochem. Cosmochim. Acta 91, 92–108.
- Özdemir, Ö., Dunlop, D.J., 2014. Hysteresis and coercivity of hematite. J. Geophys. Res. Solid Earth 119, 2582–2594. https://doi.org/10.1002/2013JB010739.
- Partin, J.W., et al., 2013. Multidecadal rainfall variability in South Pacific Convergence Zone as revealed by stalagmite geochemistry. Geology 41, 1143–1146.
- Pattnayak, K.C., Tindall, J.C., Brienen, R.J.W., Barichivich, J., Gloor, E., 2019. Can we detect changes in Amazon forest structure using measurements of the isotopic composition of precipitation? Geophys. Res. Lett. 46, 2019GL084749.
- Peel, M.C., Finlayson, B.L., McMahon, T.A., 2007. Updated world map of the Köppen-Geiger climate classification. Hydrol. Earth Syst. Sci. 11, 1633–1644. https://doi.org/10.5194/hess-11-1633-2007.
- Ponte, J.M., Font, E., Veiga-Pires, C., Hillaire-Marcel, C., Ghaleb, B., 2017. The effect of speleothem surface slope on the remanent magnetic inclination. J. Geophys. Res. Solid Earth 122, 4143–4156.
- Railsback, L.B., Akers, P.D., Wang, L., Holdridge, G.A., Voarintsoa, N.R., 2013. Layer-bounding surfaces in stalagmites as keys to better paleoclimatological histories and chronologies. Int. J. Speleol. 42, 167–180.
- Regattieri, E., et al., 2019. Holocene Critical Zone dynamics in an Alpine catchment inferred from a speleothem multiproxy record: disentangling climate and human influences. Sci. Rep. 9, 17829 https://doi.org/10.1038/s41598-019-53583-7.
- Riechelmann, D.F., Deininger, M., Scholz, D., Riechelmann, S., Schröder-Ritzrau, A., Spötl, C., Richter, D.K., Mangini, A., Immenhauser, A., 2013. Disequilibrium carbon and oxygen isotope fractionation in recent cave calcite: Comparison of cave precipitates and model data. Geochimica et Cosmochimica Acta 103, 232–244.
- Selah, A., Fryrear, D.W., 1995. Threshold wind velocities of wet soils as affected by wind blown sand. Soil Sci. 160, 304–309. https://doi.org/10.1097/00010694-199510000-00009.

- Shi, T., Ding, J., Zhu, Z., Zhang, H., Huang, J., 2022. Occurrence and distribution patterns of magnetic particles within stalagmite growth laminae. G-cubed 23. https://doi.org/10.1029/2022GC010487 e2022GC010487.
- Strauss, B.E., Strehlau, J.H., Lascu, I., Dorale, J.A., Penn, R.L., Feinberg, J.M., 2013. The origin of magnetic remanence in stalagmites: observations from electron microscopy and rock magnetism. G-cubed 14, 2013GC004950.
- Stríkis, N.M., Buarque, P.F.S.M., Cruz, F.W., Bernal, J.P., Vuille, M., Tejedor, E., Santos, M.S., Shimizu, M.H., Ampuero, A., Du, W., Sampaio, G., 2024. Modern anthropogenic drought in Central Brazil unprecedented during last 700 years. Nature Communications 15 (1), 1728.
- Treble, P., Shelley, J.M.G., Chappell, J., 2003. Comparison of high resolution sub-annual records of trace elements in a modern (1911–1992) speleothem with instrumental climate data from southwest Australia. Earth Planet Sci. Lett. 216, 141–153. https://doi.org/10.1016/S0012-821X(03)00504-1.
- Vera, C., et al., 2006. Toward a unified view of the American monsoon systems. J. Clim. 19, 4977–5000. https://doi.org/10.1175/JCLI3896.1.
- Verosub, K.L., Roberts, A.P., 1995. Environmental magnetism: past, present, and future. J. Geophys. Res. 100, 2175–2192.

- Vuille, M., Werner, M., Bradley, R.S., Keimig, F., 2005. Stable isotopes in precipitation in the Asian monsoon region. J. Geophys. Res. Atmos. 110 https://doi.org/10.1029/ 2005 DD006022
- Wang, H., Weiss, B.P., Bai, X.-N., Downey, B.G., Wang, J., Wang, J., Suavet, C., Fu, R.R., Zucolotto, M.E., 2017. Lifetime of the solar nebula constrained by meteorite paleomagnetism. Science 355, 623–627. https://doi.org/10.1126/science.aaf5043.
- Wong, C.I., Banner, J.L., Musgrove, M., 2011. Seasonal dripwater Mg/Ca and Sr/Ca variations driven by cave ventilation: implications for and modeling of speleothem paleoclimate records. Geochem. Cosmochim. Acta 75, 3514–3529.
- Yang, Q., Scholz, D., Jochum, K.P., Hoffmann, D.L., Stoll, B., Weis, U., Schwager, B., Andreae, M.O., 2015. Lead isotope variability in speleothems—a promising new proxy for hydrological change? First results from a stalagmite from western Germany. Chem. Geol. 396, 143–151. https://doi.org/10.1016/j. chemgeo.2014.12.028.
- York, D., Evensen, N.M., Martinez, M.L., De Basabe Delgado, J., 2004. Unified equations for the slope, intercept, and standard errors of the best straight line. Am. J. Phys. 72, 367–375. https://doi.org/10.1119/1.1632486.
- Zhu, Z., Feinberg, J.M., Xie, S., Bourne, M.D., Huang, C., Hu, C., Cheng, H., 2017. Holocene ENSO-related cyclic storms recorded by magnetic minerals in speleothems of central China. Proc. Natl. Acad. Sci. USA 114, 852–857.

Supplemental Figure, S1:

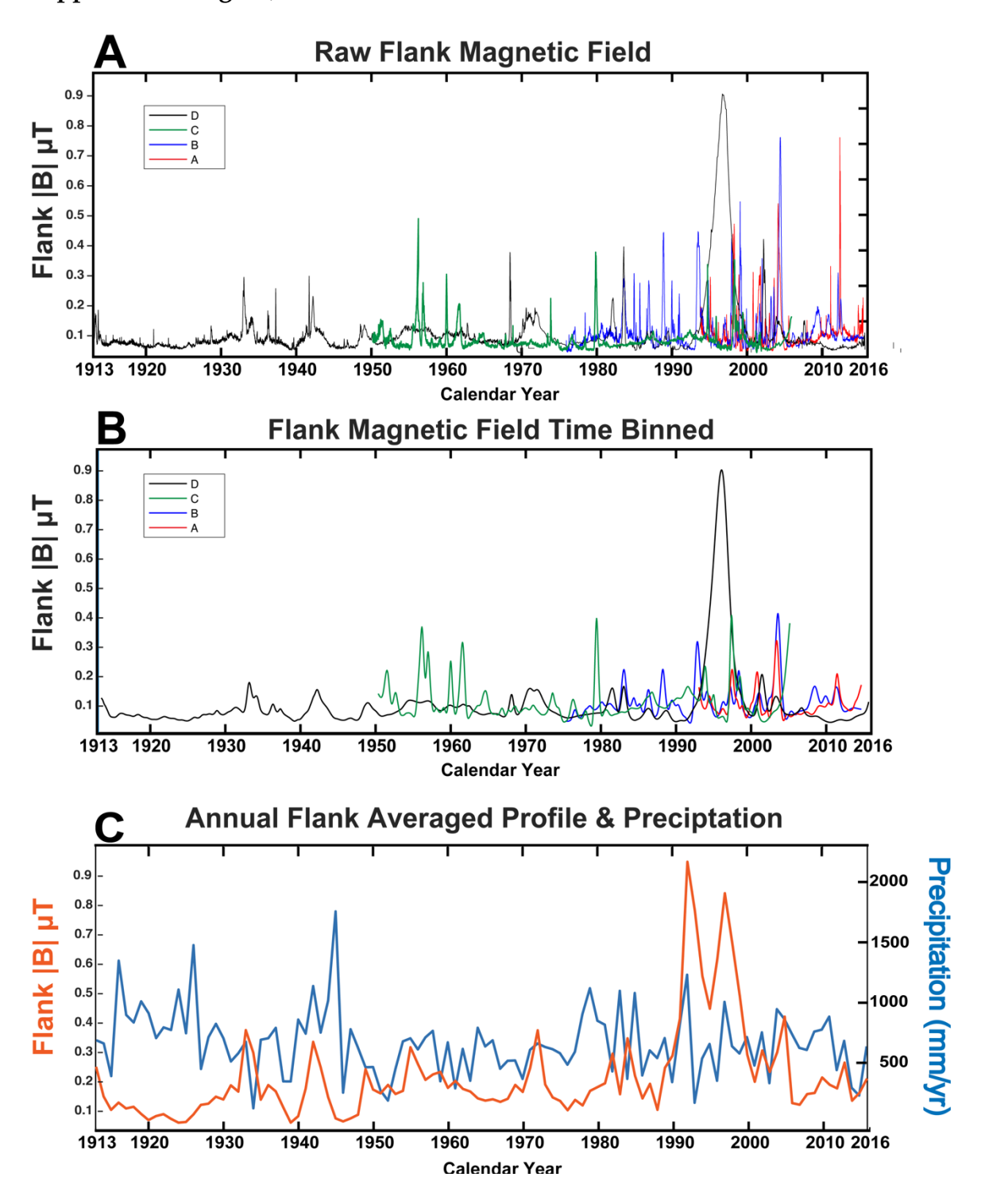


Figure S1: Plots of raw flank magnetic field time series. (**A**) The raw magnetic field time series from all four transects. Flank D-A correlate to the transect locations denoted in Fig. 2A. (**B**) Flank magnetic field data after annual binning and smoothed using a penalized spline with p=0.9, which is different from central column analysis in the Main Text in order to show finer features. (**C**) Annually binned flank magnetic field data with annual precipitation data.

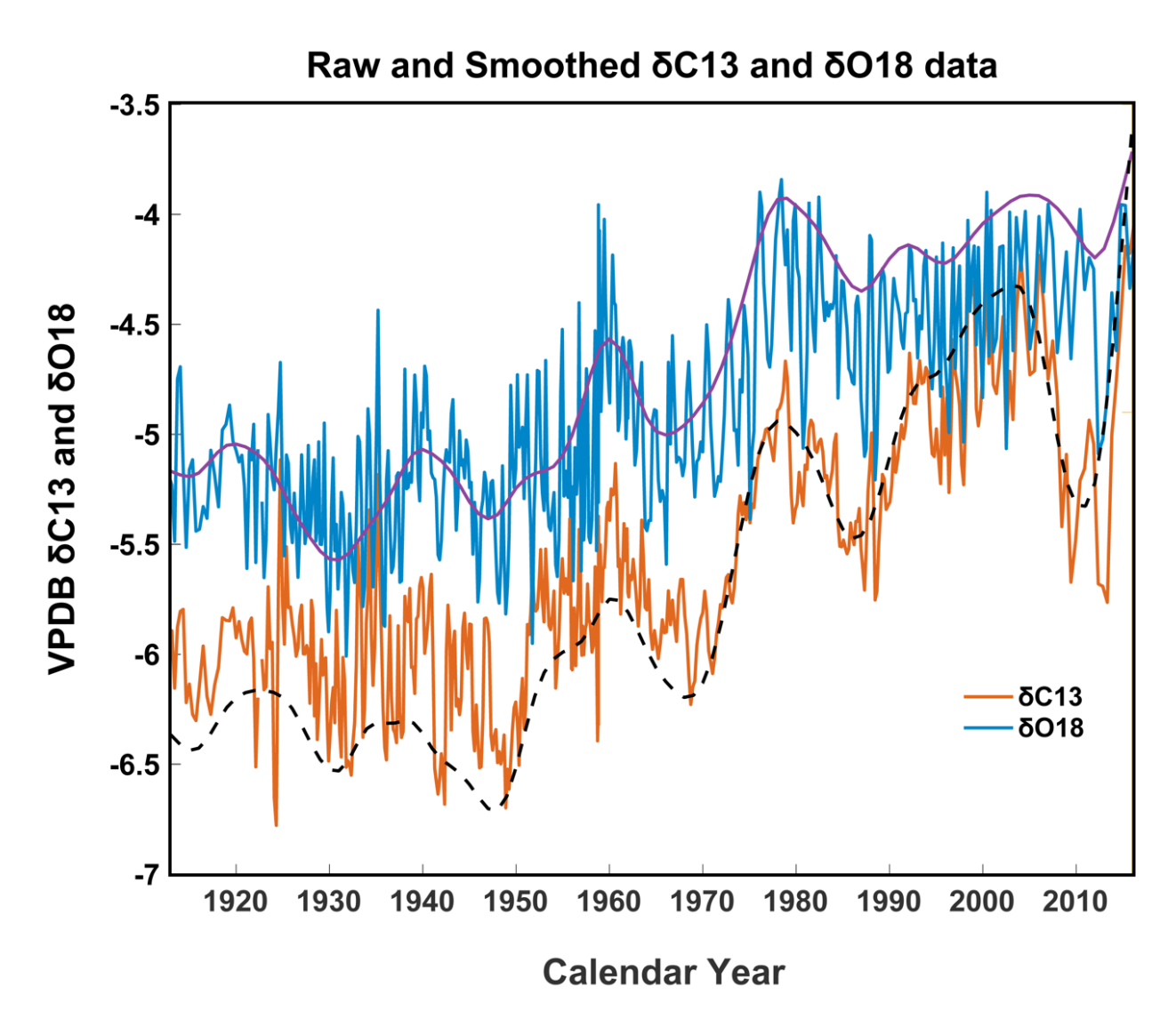


Figure S2: Plots of δ^{18} O, δ^{13} C, raw and smoothed data from Onça 2 speleothem. The data collected are from a different speleothem located in close proximity to the speleothem used in this study.

Supplemental Figure, S3:

Sample Preparation

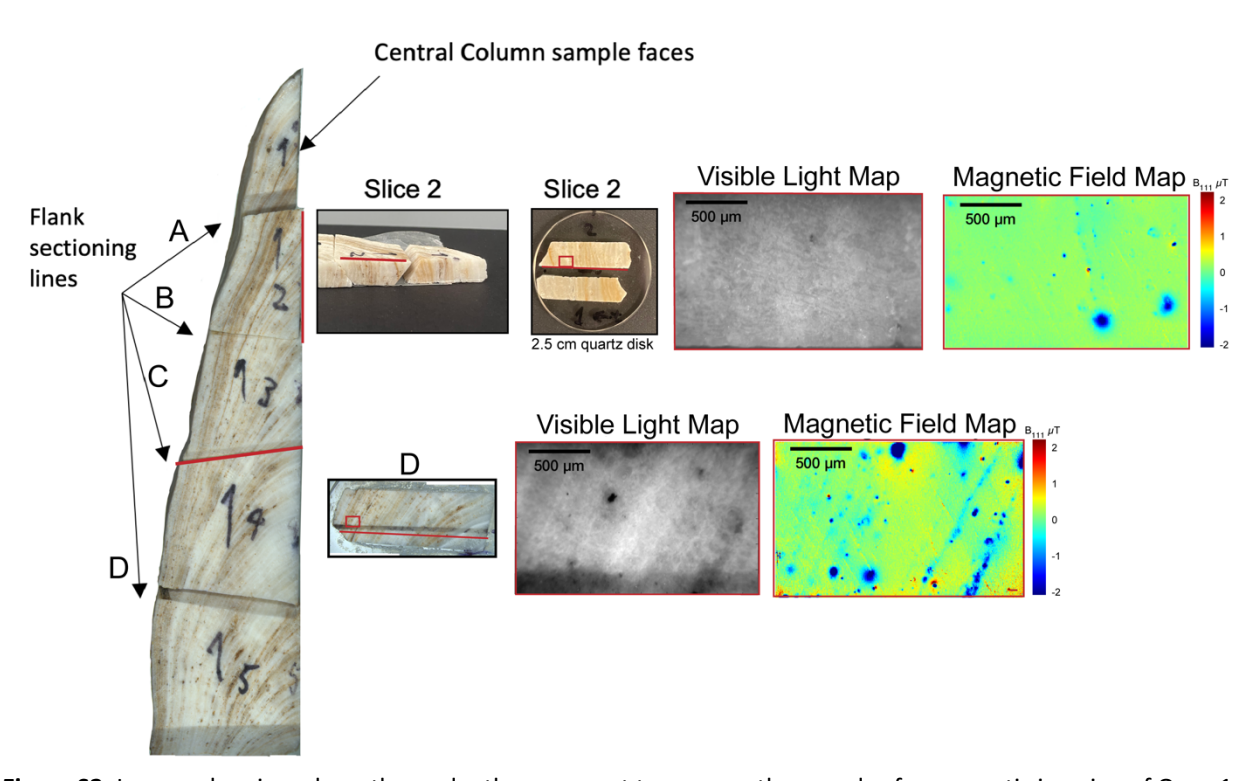


Figure S3: Images showing where the speleothem was cut to prepare the samples for magnetic imaging of Onça 1. The red lines correspond to the lines in the images immediately to the right. The top series details the central column slice 2, and the bottom series presents flank transect 4CD. The visible light maps are taken using the same optical train as the QDM magnetic field maps and are pixel-registered to the corresponding magnetic field map. A portion of the Slice 2 magnetic time series is presented in Fig. S4.

Supplemental Figure, S4:

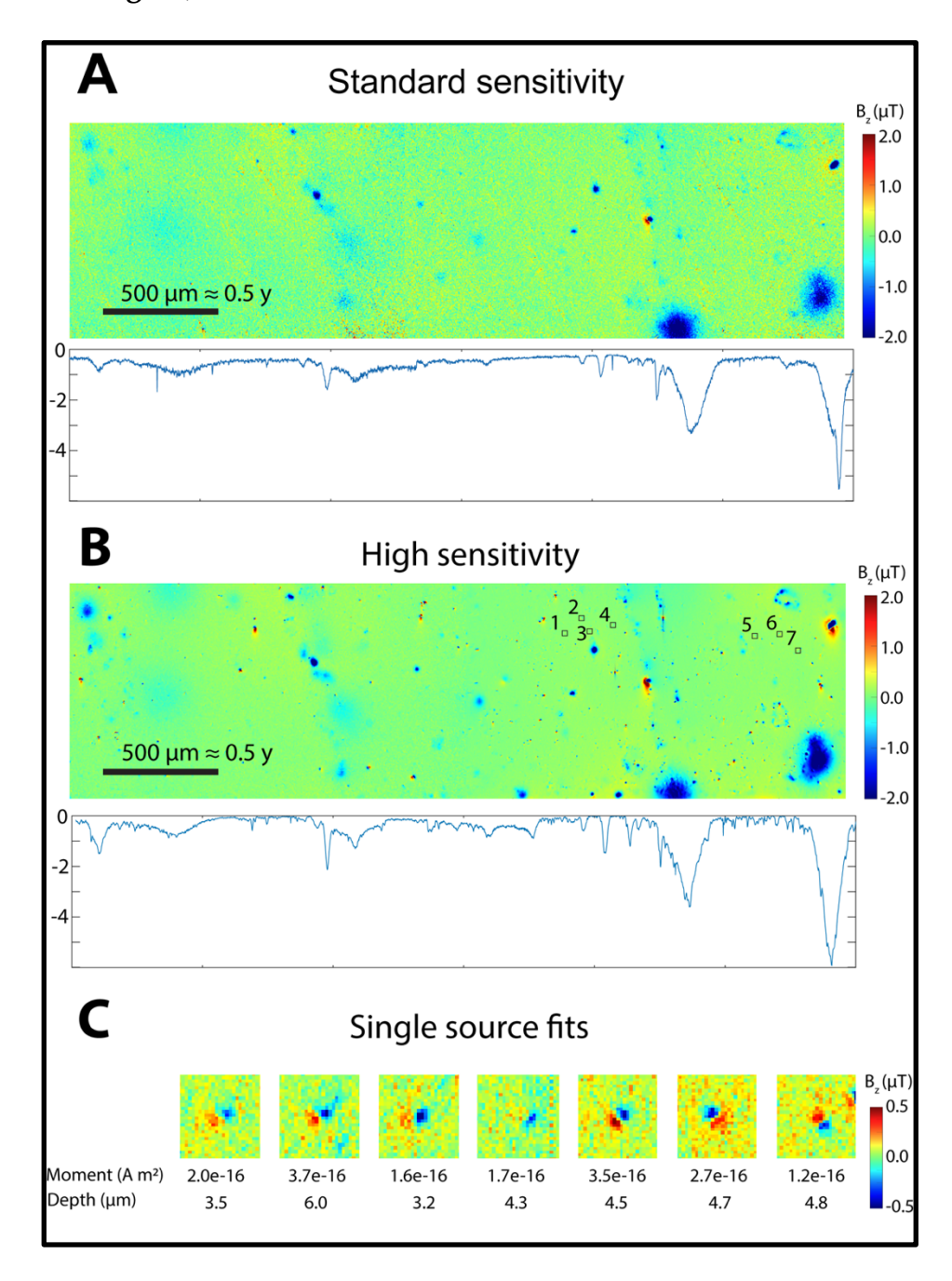


Figure S4: Comparison of **(A)** standard- and **(B)** high-sensitivity QDM datasets. We observed many more isolated small grains in the high-sensitivity mode QDM maps, although the overall time series are still dominated by laminae-scale features that are reproduced in both maps. **(C)** Seven dipole inversions of fine sources from the high-sensitivity maps highlighting detection threshold of the QDM and the sub-surface location of sources. Most of the small grains highlighted in the boxed regions appear to have higher coercivities, consistent with hematite or goethite, as they do not point in the 1 T IRM direction, which is into-the-page.

Supplemental Figure, S5:

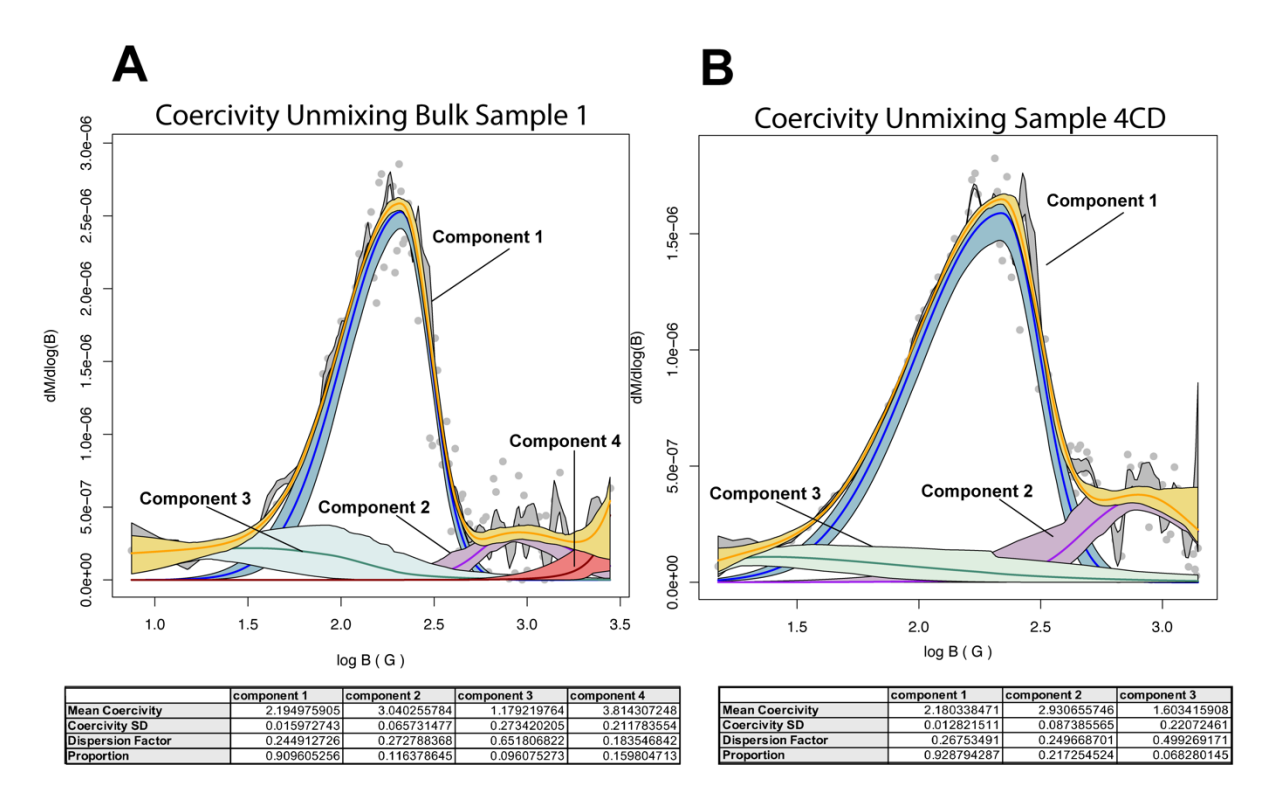


Figure S5: Coercivity unmixing models based on the MAX UnMix web application for unmixing magnetic coercivity distributions (Maxbauer, 2016). Fitted values for population mean coercivity, standard deviation of coercivity, dispersion factor, and proportion of total are given for each sample. In both cases, the yellow curve represents the combination of all fitted components. **(A)** Analysis of bulk sample from the speleothem central column. Components 1 and 2 (blue and purple) correspond to pedogenic magnetite and hematite based on our ARM susceptibility, ARM MDF, and thermal demagnetization experiments. **(B)** Analysis of a flank sample, showing largely the same grain populations.

Supplemental Figure, S6:



Figure S6: Onça 1 full speleothem before sampling.

Supplemental Figures, S7: Images of Onça Cave and Sampling Site

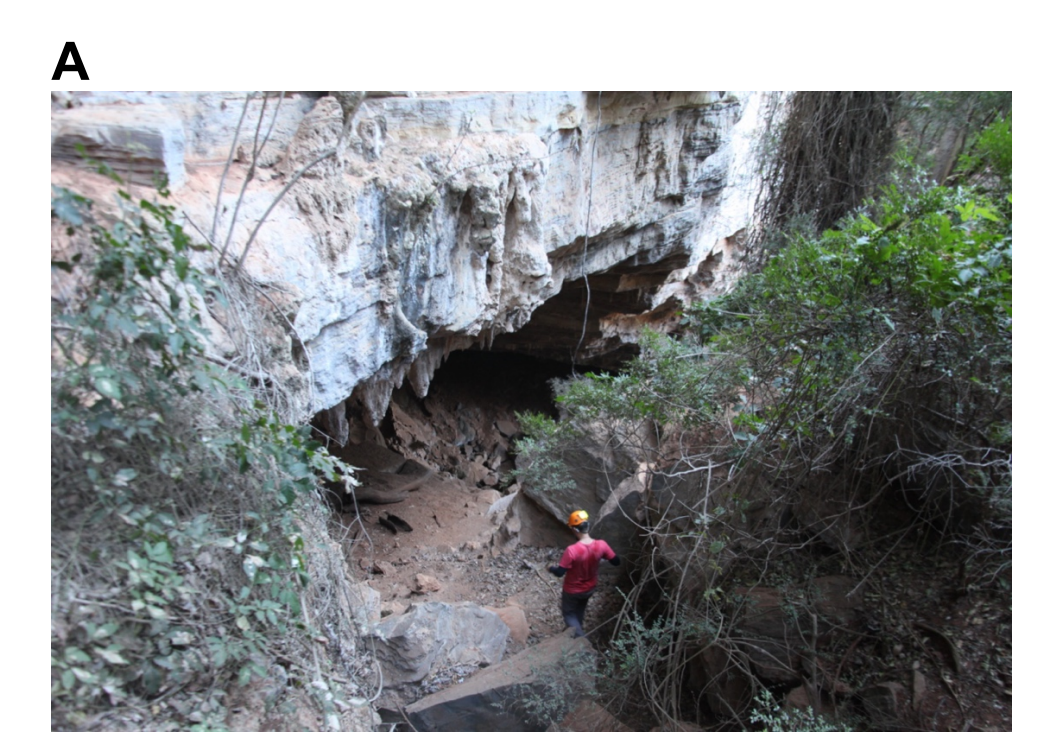


Figure S7, (A): Onça cave from the trail above the cave entrance.



Figure S7, (B): Onça cave entrance.



Figure S7, (C): Another look at the sampling site and proximity to the cave entrance.

Supplemental Figure, S8:

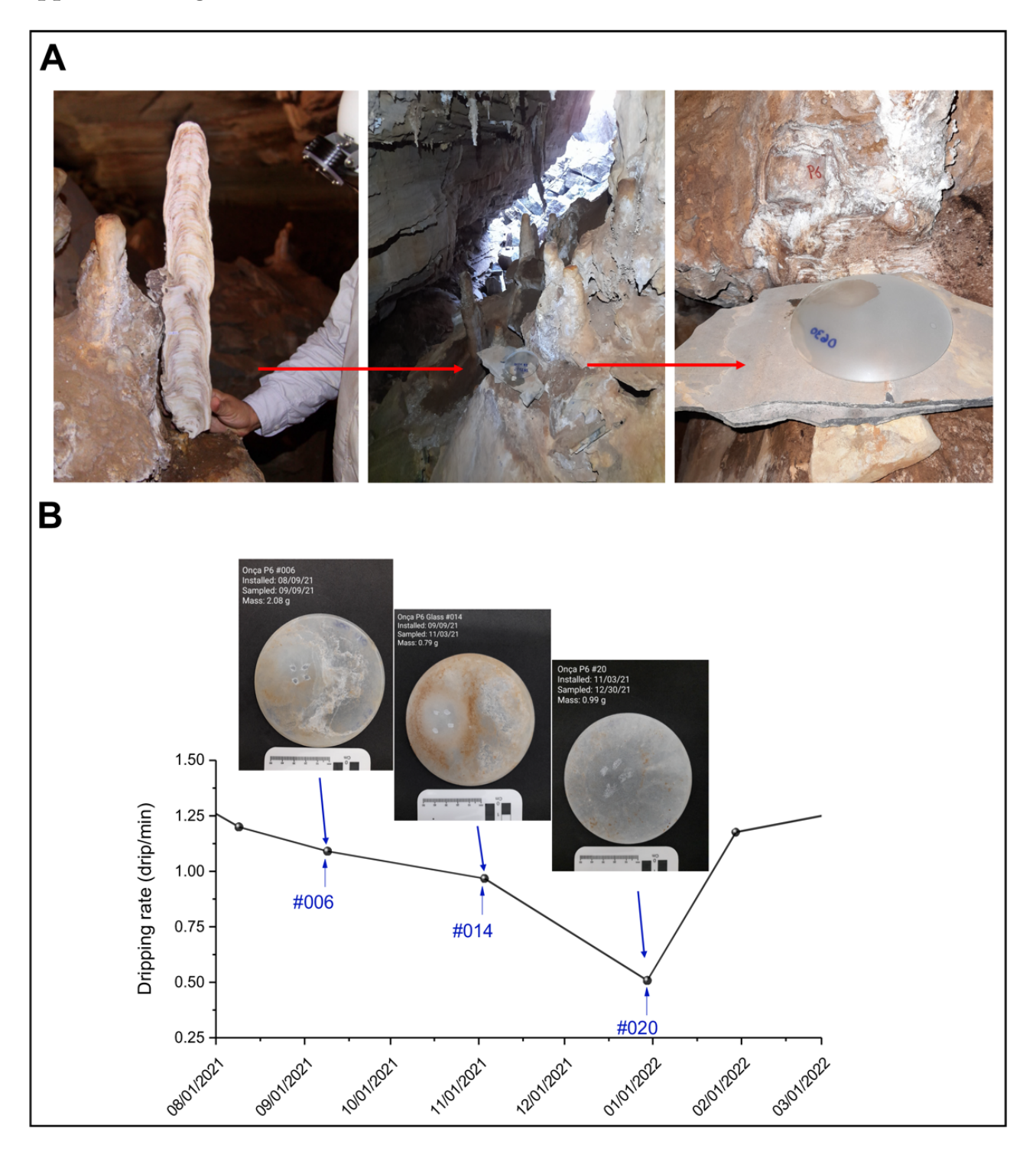


Figure S8: Farmed calcite experiment. **(A)** Images of the sampling site and placement of the collection surfaces. **(B)**Three of the glasses collected showing both the high deposition rate and accumulation of large detrital particles.

Supplemental Figure, S9:

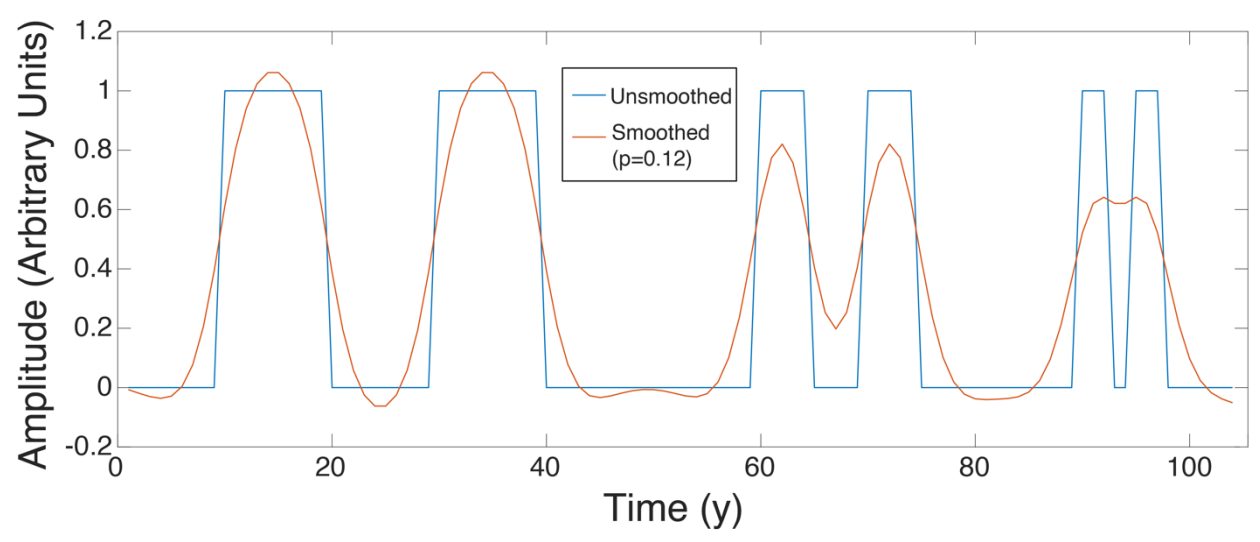


Figure S9: Empirical benchmarking of the penalized spline smoothing factor. The smoothing factor of 0.12 and the time series length and sampling frequency are identical to those of the central column magnetic field, precipitation, and stable isotope time series. The initial interval of the three sets of synthetic signals are 10, 5, and 3 y.

Supplemental Table, S1:

Sample	Depth	²³⁸ U	²³² Th	²³⁰ Th / ²³² Th	d ²³⁴ U*
Number	(mm)	(ppb)	(ppt)	(atomic x10 ⁻⁶)	(measured)
ONÇA1-1 INF	1 mm	5847±24.4	2496±51	6±0	1153.4±4.8
ONÇA1 -10 INF	10 mm	5052±21.3	842±17	23±1	1150.0±4.3
ONÇA1 -53 INF	53 mm	4817±11.4	542±11	163±5	1138.7±2.7
ONÇA1 -127 INF	127 mm	6466±20.9	621±13	417±10	1142.5±3.2
		²³⁰ Th / ²³⁸ U	²³⁰ Th Age (yr)	²³⁰ Th Age (yr)	d ²³⁴ U _{Initial} **
		(activity)	(uncorrected)	(corrected)	(corrected)
ONÇA1 -1 INF	1 mm	0.0002±0	8±1	2±4	115±5
ONÇA1 -10 INF	10 mm	0.000±0	12±1	10±2	1150±4
ONÇA1 -53 INF	53 mm	0.0011±0	57±1	55±2	1139±3
ONÇA1 -127 INF	127 mm	0.0024±0	124±2	122±2	1143±3
		²³⁰ Th Age (yr	²³⁰ Th Age		
		BP)***	(corrected)		
		(corrected)	b2k		
ONÇA1-1 INF	1 mm	-66±4	2016±4		
ONÇA1-10 INF	10 mm	-58±2	2008±2		
ONÇA1-53 INF	53 mm	-13±2	1963±2		
ONÇA1-127 INF	127 mm	54±2	1896±2		

Notes:

U decay constants: $l_{238} = 1.55125 \times 10^{-10}$ (Jaffey et al., 1971) and $l_{234} = 2.82206 \times 10^{-6}$ (Cheng et al., 2013).

Th decay constant: I230 = 9.1705x10-6 (Cheng et al., 2013).

Corrected 230 Th ages assume the initial 230 Th/ 232 Th atomic ratio of 4.4 $\pm 2.2 \times 10^{-6}$. Those are the values for a material at equilibrium, with the bulk earth 232 Th/ 238 U value of 3.8. The errors are arbitrarily assumed to be 50%.

***B.P. stands for "Before Present" where the "Present" is defined as the year 1950 A.D.

Errors given are 2σ .

Powders collected by micro-milling from the Onça 1 sample were measured using ICP-MS at the Institute of Global Environmental Change, Xi'an Jiaotong University, China laboratory.

^{*} $d^{234}U = ([^{234}U/^{238}U]_{activity} - 1)x1000.$

^{**} $d^{234}U_{initial}$ was calculated based on 230 Th age (T), i.e., $d^{234}U_{initial} = d^{234}U_{measured} \times e^{i234xT}$.